Three-dimensional multi-physics simulation and sensitivity analysis of cyclic energy storage in salt caverns

Honório, Hermínio T.; Hajibeygi, Hadi

DOI
10.1016/j.ijhydene.2024.11.081

Publication date
2024

Document Version
Final published version

Published in
International Journal of Hydrogen Energy

Citation (APA)
Honório, H. T., & Hajibeygi, H. (2024). Three-dimensional multi-physics simulation and sensitivity analysis of cyclic energy storage in salt caverns. *International Journal of Hydrogen Energy*, *94*, 1389-1405. https://doi.org/10.1016/j.ijhydene.2024.11.081

International Journal of Hydrogen Energy 94 (2024) 1389–1405

Contents lists available at ScienceDirect

International Journal of Hydrogen Energy

journal homepage: www.elsevier.com/locate/he

Three-dimensional multi-physics simulation and sensitivity analysis of cyclic energy storage in salt caverns

Hermínio T. Honório *, Hadi Hajibeygi

Faculty of Civil Engineering and Geosciences, Delft University of Technology, Stevinweg 1, 2628CN, Delft, The Netherlands

ARTICLE INFO

Keywords:
Salt rock
Salt cavern simulation
Constitutive model
Viscoplasticity
Model calibration
Underground hydrogen storage

ABSTRACT

Large-scale storage technologies are crucial to balance consumption and intermittent production of renewable energy systems. One of these technologies can be developed by converting the excess energy into compressed air or hydrogen, i.e., compressed gas, and storing it in underground solution-mined salt caverns. Salt caverns are proven seals towards compressed air and hydrogen. However, several challenges, including fast injection/production cycles and operation of systems of caverns, are yet to be resolved to allow for a safe scale-up of energy storage in salt caverns. To address these challenges, it is important to identify key parameters that impact both the safety and efficiency of the operations. For this purpose, the present study conducts sensitivity analyses to show the importance of different parameters on the time-dependent mechanical behavior of salt caverns, individually and in a multi-cavern system. The impact of different deformation mechanisms (e.g. transient and reverse creep), model calibration, cavern shape, presence of interlayers and multi-cavern interactions are investigated in this study. The constitutive model adopted in this work and the mathematical formulation are presented in detail. Additionally, an open-source three-dimensional simulator, named "SafeInCave", is developed for the numerical solution of the non-linear governing equations. The findings provide insights into improving the reliability of numerical simulations for the safe and efficient operation of salt caverns in energy storage applications.

1. Introduction

A critical challenge for decarbonizing the energy mix is to develop large-scale storage technologies that allow for balancing the consumption and the intermittent production in a seasonal time scale [1]. For instance, 17% of the wind energy produced in China in 2017 was wasted due to the production–consumption imbalance [2]. One of the alternatives to address this challenge is to store the excess energy in the form of mechanical energy. This category comprises, for instance, pumped hydro energy storage systems (PHES) [3], liquefied air energy storage (LAES) [4] and compressed air energy storage (CAES) [5]. Another promising technique is to use the excess energy to produce hydrogen molecules (chemical energy) which can be stored in underground reservoirs. Although depleted gas reservoirs are promising for large-scale energy storage [6], salt caverns are indeed recognized as the most viable option for several reasons. First of all, salt caverns have been used since the 1940s [7] for storage of various fluids such as crude oil and its derivatives [8,9], natural gas [10], compressed air [11], hydrogen [12], radioactive fluids [13], and carbon dioxide [14]. The extremely low porosity and permeability of salt rocks [15] make salt caverns an almost perfect seal, especially for hydrogen storage. In addition, creep and self-healing are favorable rock salt properties that promote cavern stability. However, fast injection/production cycles imposed on salt caverns and the necessity of scaling up these storage systems need to be carefully investigated to ensure safe and efficient operations. For this purpose, lab-scale experiments, development and calibration of constitutive models, cavern-scale simulations, and field monitoring must be integrated into a well-designed workflow, as depicted in Fig. 1.

Understanding the time-dependent mechanical behavior of salt rocks under relevant stress conditions is the first step to developing constitutive models that can be later integrated into salt cavern simulators. Generally, a salt rock sample shows transient (primary) and steady-state (secondary) creep in response to an imposed constant loading condition. When the sample is unloaded, reverse (transient) creep is also observed. If the stress state lies in the dilatancy region, long-term brittle failure may occur due to the unstable creation of micro-cracks (tertiary creep), and both permeability and volume are increased [16–19]. Conversely, micro-cracks can be suppressed if the salt rock operates in the compressibility region in a process called self-healing [20,21]. These phenomena are manifestations of different

* Corresponding author.
E-mail address: H.TasinafoHonorio@tudelft.nl (H.T. Honório).

https://doi.org/10.1016/j.ijhydene.2024.11.081
Received 24 July 2024; Received in revised form 29 September 2024; Accepted 4 November 2024
Available online 18 November 2024

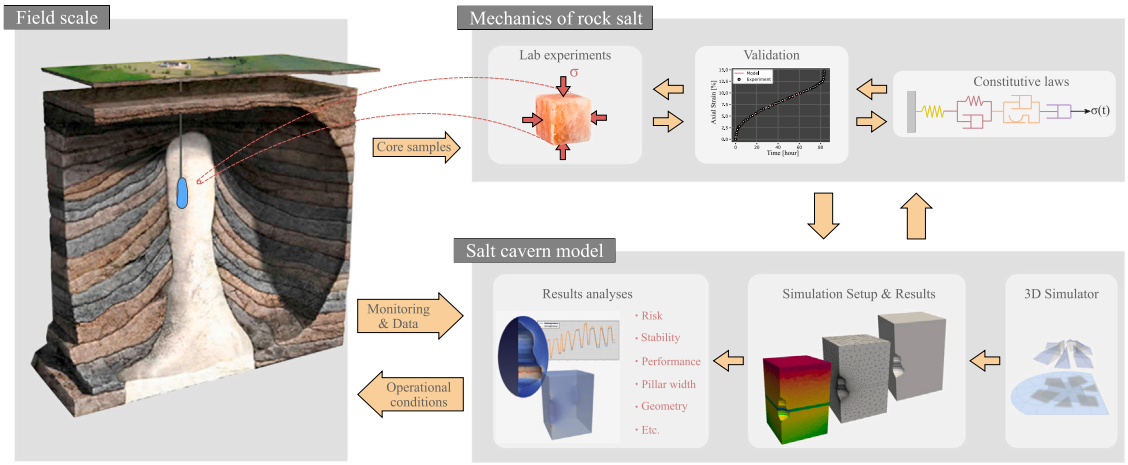

Fig. 1. Schematic overview of the modeling and simulation workflow for salt cavern systems.

microscopic mechanisms taking place within the salt crystal lattice, such as dislocation climb, dislocation glide, cross-slip, and solution precipitation [22–25]. Transient creep, for instance, is caused by a temporary imbalance between the creation and recovery of dislocation movement, whereas steady-state creep is observed when these processes balance each other [26]. These time-dependent microscopic processes are influenced by both stress and temperature conditions. Moreover, the loading rate and cyclic loading (fatigue) are also shown to affect salt rock mechanical behavior [27–31].

The complexities associated with salt rock mechanics render the constitutive modeling development a challenging task. Ideally, constitutive models should be developed based on a thorough understanding of the microscopic processes as it provides more confidence when extrapolating results outside the range of experimental conditions. This is the case for pressure solution [24,32] and dislocation creep, for which well-established theoretical constitutive models are available and are shown to provide reliable predictions. However, the remaining deformation mechanisms – transient (and reverse) creep, tertiary creep, dilation, self-healing, etc – are much more complex to understand at a microscopic level, and a phenomenological (or empirical) approach is often adopted. Besides these complexities, these deformation mechanisms are not all equally important, which is why most authors avoid including all phenomena at once. The widely used LUBBY2 model, for instance, describes only transient and steady-state creep by considering Burger's model with stress-dependent viscosities for the dashpots [33]. The Hou/Lux-ODS model was developed to overcome some of LUBBY2's limitations related to hardening and recovery, and Hou/Lux-MDS includes damage and healing processes [34]. The Munson–Dawson (M–D) constitutive model was originally developed for the WIPP salt, and it describes transient creep and three different mechanisms for steady-state creep [35]. Later modifications of this model include reverse creep [36], Hosford equivalent stress [37], damage and healing [38]. The transient creep formulation of the M-D model was also combined with the double-mechanisms creep law [39], originating the so-called enhanced double-mechanism law using transient function (EDMT model) [40]. In the Composite Dilatancy Model (CDM), besides transient and steady-state creep, dilatant behavior of salt rock is described, including the effect of humidity on creep [41]. In [42], the Norton creep law was effectively modified to capture volumetric changes in the dilatancy region, and transient creep was modeled using Perzyna's formulation with Desai's yield surface [43]. The list of models is extensive, but some important models still deserve to be mentioned [44–46]. Also worth mentioning are models including damage [47,48] and fatigue effects [49] in salt rocks.

The number of material parameters within a constitutive model increases naturally as more deformation mechanisms are included. For instance, the viscoplastic model of Desai [43], the Hou/Lux-ODS and Hou/Lux-MDS [34] depend on 11, 11 and 18 material parameters, respectively. As another example, in [37] it is stated that it is not clear how some of the parameters in the initial M-D model have been calibrated, thus new calibrations had to be performed. This represents a serious challenge for model calibration and many laboratory experiments are required. For this reason, some authors decide to keep well-established (calibrated) models and add new features (e.g. transient creep) as necessary [40]. In [50], a general calibration strategy is proposed based on an optimization framework in which new experiments can be added as they are made available. Although the impact of model calibration against laboratory experiments can be readily assessed, studies on its impacts on salt cavern simulations are not reported in the literature.

Salt cavern simulations, like any other numerical analysis, are designed to investigate particular problems associated with the different stages of the cavern life-cycle (i.e., construction, operation and abandonment). The cavern leaching, debrining, and operational phases were simulated in [42], where different stability criteria were also analyzed. Cavern volumetric convergence is usually analyzed during the operation stage [15,35,37,51]. The subsidence is also a concern during cavern operation and especially after abandonment [51,52]. Due to salt creep, borehole and casing stability is also a concern [53,54]. Other studies focus on cavern stability and risk assessment in bedded salt formations, system of caverns and proximity of fractures [15,48,51,55–58]. Cyclic operations, which are particularly relevant for renewable energy storage, have been investigated in many studies [49,59–61]. However, few parametric studies have been conducted to investigate, for example, the importance of pressure solution creep [51,62], the impact of interlayers and cavern complex geometries [63].

Designing relevant simulations and ensuring cost-effective and reliable results are the main challenges faced in numerical analyses. The quality of salt cavern simulations can be measured by the distance between the simulation results and field measurements (i.e., reality). This distance[1] is affected by many variables, such as the choice of appropriate constitutive models and numerical schemes, appropriate lithological characterization, cavern geometries, boundary conditions, etc. Characterization of the impact of these variables on the salt cavern deformation is crucial in designing computationally affordable yet reliable simulations. Although many numerical studies in the literature consider different components of the full-physics deformation process

[1] If this distance is interpreted as a function to be minimized, sensitivity analysis allows us to identify which direction to move in order to improve results. From this perspective, sensitivity analysis can be compared to computing partial derivatives of a function.

(e.g. transient creep, pressure solution creep, tertiary creep, presence of interlayers in bedded formations, mutual interactions in systems of caverns, etc.), they do not intend to assess the impact of each of these components individually on the overall simulation results. During the design of models for salt caverns, lack of understanding of the importance of each of these components can either result in an overly detailed (and expensive) model or a model that is insufficiently representative (thus inaccurate and unreliable). In this context, the present work conducts sensitivity analyses to investigate the impact of different mechanism in simulation of salt cavern deformations under cyclic operations. The main contribution of this study is to investigate the impact of model calibration, transient and reverse creep, cavern geometry, non-salt interlayers, and mutual interaction in systems of caverns. For this purpose, an open-source three-dimensional finite element simulator named "SafeInCave" has been also developed to include a salt rock constitutive model that considers transient, reverse and steady-state creep, which is also a relevant contribution of this work.

The remainder of this manuscript is organized as follows. Section 2 describes the governing equations and the constitutive model adopted to describe salt rock mechanics. The numerical formulation is presented in Section 3, which includes description of the time integration schemes, stress linearization (consistent tangent matrix), numerical treatment of each element of the constitutive model, and the weak form for the finite element formulation. Next, Section 4 describes the different constitutive model variations adopted in our analyses, the cavern geometries, boundary conditions (pressure schedules), initial conditions, and sets of material properties used. In the results section (Section 5), each analysis is appropriately described based on the information provided in Section 4, and the obtained results are shown and discussed. Finally, the main conclusions are summarized in Section 6.

2. Mathematical model

The mechanical behavior of salt caverns is described by the linear momentum equilibrium equation, which reads

$$\nabla \cdot \boldsymbol{\sigma} = \mathbf{f}, \tag{1}$$

where $\boldsymbol{\sigma}$ is the stress tensor and $\mathbf{f}$ is the external force per volume vector. Constitutive laws are required to relate the stress tensor $\boldsymbol{\sigma}$ to the total strain tensor $\boldsymbol{\varepsilon}$. In this work, we adopt the same constitutive model as in [50], which considers an elastic element ($\boldsymbol{\varepsilon}_e$) for instantaneous elastic response, a viscoelastic ($\boldsymbol{\varepsilon}_{ve}$) element for reverse creep, a viscoplastic ($\boldsymbol{\varepsilon}_{vp}$) element for transient creep, and a dashpot for steady-state creep due to dislocation movement. Fig. 2 illustrates the complete constitutive model, where the non-elastic strain tensor is defined as the summation of all elements except the elastic one. In this manner, the stress tensor can be written as

$$\boldsymbol{\sigma} = \mathbb{C}_0 : \left(\boldsymbol{\varepsilon} - \boldsymbol{\varepsilon}_{ne}\right), \tag{2}$$

where $\mathbb{C}_0$ is the 4th-order stiffness tensor associated with the spring (elastic) element. The non-elastic strain tensor is given by the summation of all non-elastic elements, N_{ne}, i.e.,

$$\boldsymbol{\varepsilon}_{ne} = \sum_{i=1}^{N_{ne}} \boldsymbol{\varepsilon}_i. \tag{3}$$

It is clear that computing the total non-elastic strains $\boldsymbol{\varepsilon}_{ne}$ for each element is required for obtaining the stress tensor in Eq. (2). In the subsections below, the individual non-elastic strain rates are defined.

2.1. Viscoelastic element

An external stress $\boldsymbol{\sigma}$ acting on the viscoelastic element (also called Kelvin–Voigt element) is counter-balanced by the stresses acting on its spring and dashpot, i.e.,

$$\boldsymbol{\sigma} = \underbrace{\mathbb{C}_1 : \boldsymbol{\varepsilon}_{ve}}_{\text{spring}} + \underbrace{\eta_1 \dot{\boldsymbol{\varepsilon}}_{ve}}_{\text{dashpot}} \quad \Rightarrow \quad \dot{\boldsymbol{\varepsilon}}_{ve} = \frac{1}{\eta_1}\left(\boldsymbol{\sigma} - \mathbb{C}_1 : \boldsymbol{\varepsilon}_{ve}\right), \tag{4}$$

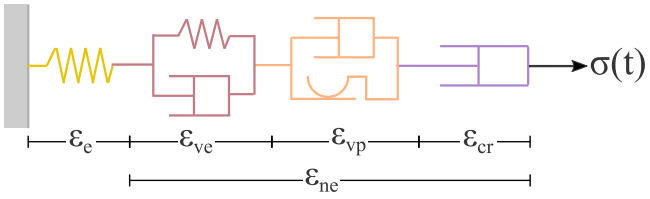

Fig. 2. Elements composing the constitutive model.

where $\mathbb{C}_1$ and η_1, respectively, denoting the 4th-order stiffness tensor and viscosity associated with the spring and dashpot of the viscoelastic element.

2.2. Viscoplastic element

For the viscoplastic contribution, the strain rate is computed following an associated flow-rule and the classical Perzyna's viscoplastic formulation, i.e.,

$$\dot{\boldsymbol{\varepsilon}}_{vp} = \mu_1 \left\langle \frac{F_{vp}}{F_0} \right\rangle^{N_1} \frac{\partial Q_{vp}}{\partial \boldsymbol{\sigma}}, \tag{5}$$

where the yield function proposed by [43] is employed, which reads

$$F_{vp}(\boldsymbol{\sigma}, \alpha) = J_2 - \left(\gamma I_1^2 - \alpha I_1^n\right)\left[\exp\left(\beta_1 I_1\right) - \beta \cos(3\theta)\right]^m \tag{6}$$

with I_1 and J_2 respectively representing the first invariant of the stress tensor and the second invariant of its deviatoric part, and θ is Lode's angle. The hardening parameter α obeys the following hardening rule,

$$\alpha = a_1 \left[\left(\frac{a_1}{\alpha_0}\right)^{1/\eta} + \xi\right]^{-\eta}, \quad \text{where} \quad \xi = \int_{t_0}^{t} \sqrt{\dot{\boldsymbol{\varepsilon}}_{vp} : \dot{\boldsymbol{\varepsilon}}_{vp}}\,\mathrm{d}t. \tag{7}$$

In Eqs. (5), (6) and (7) the quantities μ_1, F_0, N_1, n, γ, β_1, β, m, a_1 and η are all material parameters.

To better understand the behavior of the viscoplastic model described by Eq. (5), consider a constant stress point $\boldsymbol{\sigma}$ lying outside the yield surface[2] (thus $F_{vp} > 0$), as illustrated in Fig. 3. In this case, the viscoplastic strain rate will be non-zero, causing the accumulated viscoplastic strain ξ to increase, and the hardening parameter α to decrease according to Eq. (7). The consequence of reducing α is that the yield surface ($F_{vp} = 0$) expands towards the stress state point, thus reducing the value of the yield function and consequently the strain rate. Therefore, the viscoplastic strain rate is maximum at the beginning of the viscoplastic deformation, and zero when the yield surface touches the stress point, which is precisely the expected behavior of the transient creep stage.

The yield surfaces shown in Fig. 3 are obtained through Eq. (6) by considering a certain value for Lode's angle θ, making $F_{vp} = 0$, and solving it for J_2, i.e.,

$$J_2 = \left\langle \left(\gamma I_1^2 - \alpha I_1^n\right)\left[\exp\left(\beta_1 I_1\right) - \beta \cos(3\theta)\right]^m \right\rangle. \tag{8}$$

The Macaulay brackets in Eq. (8) are used because $\sqrt{J_2}$ does not admit $J_2 < 0$. The yield surfaces in Fig. 3 were obtained by choosing $\theta = 30°$, varying the values of I_1 from -10 MPa to 130 MPa, and computing the corresponding values of $\sqrt{J_2}$. In practice, the Lode's angle is not arbitrarily chosen, but calculated based on the stress tensor at a particular point and time. This can be observed in Fig. 16, where the initial and final yield surfaces are calculated with different values of θ.

[2] The yield surface is defined as $F_{vp} = 0$

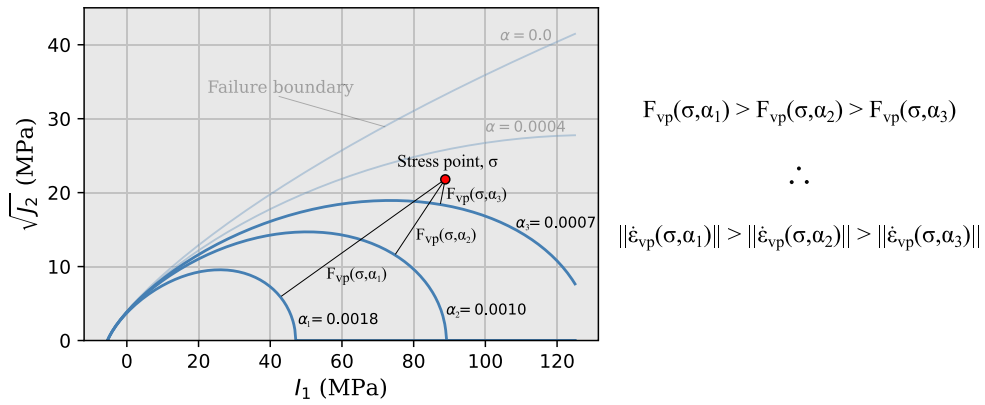

Fig. 3. Yield surface evolution due to accumulated viscoplastic strain.

2.3. Dislocation creep element

The dislocation creep contribution is represented by a simple power law in combination with Arrhenius law [63], which is written as

$$\dot{\boldsymbol{\varepsilon}}_{cr} = A \exp\left(-\frac{Q}{RT}\right) q^{n-1}\mathbf{s}, \tag{9}$$

where $\mathbf{s}$ and q are the deviatoric and von Mises stresses, respectively. Moreover, A and n are material parameters, Q is the activation energy, R is Boltzmann's constant and T is temperature.

3. Numerical formulation

As shown in the previous section, non-elastic strains are required to compute the stress tensor, but they also depend on the stress tensor itself and, potentially, on internal parameters. In other words, the stress tensor is a nonlinear function of total strain, which makes Eq. (1) a nonlinear problem to be solved. In these cases, deriving a consistent tangent matrix is essential for ensuring stable solutions for implicit time integration schemes [64]. A procedure similar to the one presented in [65] is also adopted in this work. Although the constitutive model proposed in [50] and discussed in Section 2 is used, the linearization procedure discussed below is general enough to be applied to any other constitutive model. Additionally, the numerical formulation is developed in terms of the stress $\boldsymbol{\sigma}$, instead of the increment of stress $\delta\boldsymbol{\sigma}$, to provide a clear presentation.

3.1. Stress linearization

Linearization of the stress field allows for solving Eq. (1) iteratively at each time step. Therefore, at iteration $k+1$ of the current time step, one has to solve

$$\nabla \cdot \boldsymbol{\sigma}^{k+1} = \mathbf{f}, \tag{10}$$

where

$$\boldsymbol{\sigma}^{k+1} = \mathbb{C}_0 : \left(\boldsymbol{\varepsilon}^{k+1} - \boldsymbol{\varepsilon}_{ne}^{k+1}\right). \tag{11}$$

The linearization of $\boldsymbol{\sigma}^{k+1}$ starts by integrating Eq. (11) in time between t and $t+\Delta t$. Employing the $\theta-$rule to integrate $\boldsymbol{\varepsilon}_i^{k+1}$ leads to

$$\boldsymbol{\varepsilon}_i^{k+1} = \boldsymbol{\varepsilon}_i^{t} + \phi_1 \dot{\boldsymbol{\varepsilon}}_i^{t} + \phi_2 \dot{\boldsymbol{\varepsilon}}_i^{k+1}, \tag{12}$$

where $\phi_1 = \Delta t\theta$ and $\phi_2 = \Delta t(1-\theta)$. In this case, $\theta = 1$, $\theta = 1/2$ and $\theta = 0$ provide explicit, Crank–Nicolson and fully implicit time integrations, respectively. Additionally, the superscript t denotes the variables evaluated at the previous time step t, whereas the superscript $k+1$ indicates the current iteration of the current time step $t+\Delta t$. Naturally, superscript k will indicate the previous iteration of the current time step. The superscript $t+\Delta t$ is always omitted to keep a concise notation.

In general, the non-elastic strain rate is a function of the stress tensor $\boldsymbol{\sigma}$ and an internal parameter α_i, i.e.,

$$\dot{\boldsymbol{\varepsilon}}_i = \dot{\boldsymbol{\varepsilon}}_i\left(\boldsymbol{\sigma}, \alpha_i\right). \tag{13}$$

Using Taylor series to expand Eq. (13) between two consecutive iterations leads to,

$$\dot{\boldsymbol{\varepsilon}}_i^{k+1} = \dot{\boldsymbol{\varepsilon}}_i^{k} + \frac{\partial \dot{\boldsymbol{\varepsilon}}_i}{\partial \boldsymbol{\sigma}} : \delta\boldsymbol{\sigma} + \frac{\partial \dot{\boldsymbol{\varepsilon}}_i}{\partial \alpha_i}\delta\alpha_i, \tag{14}$$

where $\delta\boldsymbol{\sigma} = \boldsymbol{\sigma}^{k+1} - \boldsymbol{\sigma}^{k}$ and $\delta\alpha_i = \alpha_i^{k+1} - \alpha_i^{k}$. The increment of the internal variable, $\delta\alpha_i$, can be obtained by using the evolution equation of α_i to define a residue function which can be generally written as

$$r_i = r_i(\boldsymbol{\sigma}, \alpha_i). \tag{15}$$

Finally, using Taylor series to expand this residue function from r_i^k to r_i^{k+1} and applying Newton–Raphson approach yields

$$\cancel{r_i^{k+1}}^{\,0} = r_i^k + \underbrace{\frac{\partial r_i^k}{\partial \alpha_i}}_{h_i}\delta\alpha_i + \frac{\partial r_i^k}{\partial \boldsymbol{\sigma}} : \delta\boldsymbol{\sigma} = 0 \quad \Rightarrow \quad \delta\alpha_i = -\frac{1}{h_i}\left(r_i^k + \frac{\partial r_i^k}{\partial \boldsymbol{\sigma}} : \delta\boldsymbol{\sigma}\right). \tag{16}$$

By combining Eqs. (14) and (16) and substituting into Eq. (12), the strain tensor of the current iteration is expressed as

$$\boldsymbol{\varepsilon}_i^{k+1} = \bar{\boldsymbol{\varepsilon}}_i^{k} + \phi_2 \mathbb{G}_i : \delta\boldsymbol{\sigma} - \phi_2 \mathbf{B}_i, \tag{17}$$

where

$$\bar{\boldsymbol{\varepsilon}}_i^{k} = \boldsymbol{\varepsilon}_i^{t} + \phi_1 \dot{\boldsymbol{\varepsilon}}_i^{t} + \phi_2 \dot{\boldsymbol{\varepsilon}}_i^{k}, \tag{18}$$

$$\mathbb{G}_i = \frac{\partial \dot{\boldsymbol{\varepsilon}}_i}{\partial \boldsymbol{\sigma}} - \frac{1}{h_i}\frac{\partial \dot{\boldsymbol{\varepsilon}}_i}{\partial \alpha_i}\frac{\partial r_i^k}{\partial \boldsymbol{\sigma}}, \tag{19}$$

$$\mathbf{B}_i = \frac{r_i^k}{h_i}\frac{\partial \dot{\boldsymbol{\varepsilon}}_i}{\partial \alpha_i}. \tag{20}$$

Finally, the non-elastic strain tensor is given by

$$\boldsymbol{\varepsilon}_{ne}^{k+1} = \sum_{i=1}^{N_{ne}} \boldsymbol{\varepsilon}_i = \bar{\boldsymbol{\varepsilon}}_{ne}^{k} + \phi_2 \mathbb{G}_{ne} : \delta\boldsymbol{\sigma} - \phi_2 \mathbf{B}_{ne}, \tag{21}$$

with $\bar{\boldsymbol{\varepsilon}}_{ne}^{k} = \sum_{i=1}^{N_{ne}} \bar{\boldsymbol{\varepsilon}}_i^{k}$, $\mathbb{G}_{ne} = \sum_{i=1}^{N_{ne}} \mathbb{G}_i$ and $\mathbf{B}_{ne} = \sum_{i=1}^{N_{ne}} \mathbf{B}_i$.

From Eq. (21), the linearized form of the stress tensor is expressed as

$$\boldsymbol{\sigma}^{k+1} = \mathbb{C}_T : \left(\boldsymbol{\varepsilon}^{k+1} - \bar{\boldsymbol{\varepsilon}}_{ne}^{k} + \phi_2 \mathbb{G}_{ne} : \boldsymbol{\sigma}^{k} + \phi_2 \mathbf{B}_{ne}\right), \tag{22}$$

where $\mathbb{C}_T = \left(\mathbb{C}_0^{-1} + \phi_2 \mathbb{G}_{ne}\right)^{-1}$. Combining Eqs. (10) and (22) and rearranging the terms, the linearized form of the momentum balance equation reads

$$\nabla \cdot \mathbb{C}_T : \boldsymbol{\varepsilon}^{k+1} = \mathbf{f} + \nabla \cdot \mathbb{C}_T : \boldsymbol{\varepsilon}_{\text{rhs}}^{k}, \tag{23}$$

where $\boldsymbol{\varepsilon}_{\text{rhs}}^{k} = \bar{\boldsymbol{\varepsilon}}_{ne}^{k} - \phi_2 \mathbb{G}_{ne} : \boldsymbol{\sigma}^{k} - \phi_2 \mathbf{B}_{ne}$.

On the right-hand side of Eq. (22), the quantities $\boldsymbol{\epsilon}_i$, $\dot{\boldsymbol{\epsilon}}_i$, $\mathbb{G}_i$ and $\mathbf{B}_i$ must be computed for all elements included in the constitutive model. The following subsections show this procedure for each element.

3.2. Viscoelastic element

An expression for the viscoelastic strain rate can be obtained by combining Eqs. (4) and (12), with $i = ve$, and solving for $\dot{\boldsymbol{\epsilon}}_{ve}$. This results in the following equations

$$\dot{\boldsymbol{\epsilon}}_{ve} = \left(\eta_1 \mathbb{I} + \phi_2 \mathbb{C}_1\right)^{-1} : \left[\boldsymbol{\sigma} - \mathbb{C}_1 : \left(\boldsymbol{\epsilon}^t_{ve} + \phi_1 \dot{\boldsymbol{\epsilon}}^t_{ve}\right)\right] \tag{24}$$

where $\mathbb{I}$ represents the 4th-order identity tensor. The derivative of Eq. (24) with respect to $\boldsymbol{\sigma}$ gives,

$$\mathbb{G}_{ve} = \frac{\partial \dot{\boldsymbol{\epsilon}}_{ve}}{\partial \boldsymbol{\sigma}} = \left(\eta_1 \mathbb{I} + \phi_2 \mathbb{C}_1\right)^{-1}. \tag{25}$$

Furthermore, the viscoelastic model has no internal variables, implying that $\mathbf{B}_{ve} = 0$. Finally, the viscoelastic strain at iteration $k+1$ can be computed as,

$$\boldsymbol{\epsilon}^{k+1}_{ve} = \boldsymbol{\epsilon}^t_{ve} + \phi_1 \dot{\boldsymbol{\epsilon}}^t_{ve} + \phi_2 \left(\dot{\boldsymbol{\epsilon}}^k_{ve} + \mathbb{G}_{ve} : \delta\boldsymbol{\sigma}\right). \tag{26}$$

3.3. Dislocation creep element

Eq. (9) gives the strain rate for the dislocation creep element. The tangent matrix is given by

$$\mathbb{G}_{cr} = \frac{\partial \dot{\boldsymbol{\epsilon}}_{cr}}{\partial \boldsymbol{\sigma}}, \tag{27}$$

where the partial derivatives are computed by finite differences. Since the dislocation creep model does not depend on internal variables ($\mathbf{B}_{cr} = 0$), the creep strain at iteration $k+1$ is computed as,

$$\boldsymbol{\epsilon}^{k+1}_{cr} = \boldsymbol{\epsilon}^t_{cr} + \phi_1 \dot{\boldsymbol{\epsilon}}^t_{cr} + \phi_2 \left(\dot{\boldsymbol{\epsilon}}^k_{cr} + \mathbb{G}_{cr} : \delta\boldsymbol{\sigma}\right). \tag{28}$$

3.4. Viscoplastic element

The viscoplastic strain rate is computed by Eq. (5), where α is an internal variable. For this reason, a residual function is defined based on the hardening rule as

$$r^k_{vp} = \alpha^k - a_1 \left[\left(\frac{a_1}{\alpha_0}\right)^{1/\eta} + \xi^k\right]^{-\eta}, \quad \text{where} \quad \xi^k = \int_{t_0}^{t} \sqrt{\dot{\boldsymbol{\epsilon}}^k_{vp} : \dot{\boldsymbol{\epsilon}}^k_{vp}}\,\mathrm{d}t \tag{29}$$

from which $h^k_{vp} = \frac{\partial r^k_{vp}}{\partial \alpha}$, as shown in Eq. (16), and Eqs. (19) and (20) are employed. All derivatives are computed by finite differences. The viscoplastic strain at iteration $k+1$ is

$$\boldsymbol{\epsilon}^{k+1}_{vp} = \boldsymbol{\epsilon}^t_{vp} + \phi_1 \dot{\boldsymbol{\epsilon}}^t_{vp} + \phi_2 \left(\dot{\boldsymbol{\epsilon}}^k_{vp} + \mathbb{G}_{vp} : \delta\boldsymbol{\sigma}\right) - \phi_2 \mathbf{B}_{vp}. \tag{30}$$

3.5. Weak formulation

Consider a domain Ω bounded by a surface Γ outward oriented by a unitary vector $\mathbf{n}$. Furthermore, consider a vector test function $\mathbf{v} \in \mathcal{V}$, where $\mathcal{V}$ is a test function space. The weak form of Eq. (23) can then be written as

$$\int_\Omega \mathbb{C}_T : \boldsymbol{\varepsilon}\left(\mathbf{u}^{k+1}\right) : \boldsymbol{\varepsilon}(\mathbf{v})\,\mathrm{d}\Omega = \int_\Omega \mathbf{f}\cdot\mathbf{v}\,\mathrm{d}\Omega + \int_\Gamma \mathbf{t}\cdot\mathbf{v}\,\mathrm{d}\Gamma + \int_\Omega \mathbb{C}_T : \boldsymbol{\epsilon}^k_{\mathrm{rhs}} : \boldsymbol{\varepsilon}(\mathbf{v})\,\mathrm{d}\Omega \tag{31}$$

where $\mathbf{t} = \boldsymbol{\sigma}\cdot\mathbf{n}$ and $\mathbf{u} \in \mathcal{V}$. Additionally, for any $\mathbf{w} \in \mathcal{V}$, the small strain assumption implies that

$$\boldsymbol{\varepsilon}(\mathbf{w}) = \frac{1}{2}\left(\nabla\mathbf{w} + \nabla\mathbf{w}^T\right). \tag{32}$$

After the finite element discretization, the weak form represented by Eq. (31) results in a linear system $\mathbf{A}\mathbf{u} = \mathbf{b}$, where $\mathbf{A}$ is the coefficient matrix, $\mathbf{b}$ is the right-hand side vector, and $\mathbf{u}$ represents the displacement vectors at the nodal points.

4. Methodology

In this work, several investigations are carried out to understand the behavior of salt caverns according to different choices made during the simulation setup. The objective is to analyze the impact of considering (i) different deformation mechanisms, (ii) different calibrations of the constitutive models for the same salt rock, (iii) regular and irregular cavern shapes, (iv) the presence of a non-salt interlayer, and (v) the presence of nearby caverns (system of caverns). In this section, we describe the constitutive models, material parameters, geometries, boundary/initial conditions, and laboratory experiments adopted in this work. The descriptions of each test case are left for the results section (Section 5).

4.1. Constitutive models

The constitutive models considered in this work are depicted in Fig. 4. Model-A includes all elements discussed in Sections 2 and 3. The viscoplastic and viscoelastic elements are removed from models B and C, respectively. Finally, Model-D only considers elastic and dislocation creep. The comparison of these constitutive models is used to assess the importance of viscoelasticity and viscoplasticity on the mechanical behavior of salt rocks.

4.2. Cavern geometries

The shape of a real salt cavern is, in general, extremely irregular, because the heterogeneity within the salt formations impact the solution mining process. Complex cavern shapes may present pockets from where the gas cannot be removed, which can be a serious problem during cavern abandonment when the gas has to be replaced by brine before the cavern is shut in. Moreover, irregular solution mining can result in unstable structures on the upper part of the cavern that can later collapse and fall to the sump, thus compromising mechanical stability and possibly causing measurable seismic activity. Although these are important consequences, in this work we focus on the effect that stress concentration regions have on creep and, therefore, cavern convergence. To measure this effect, we consider two different cavern shapes, as shown in Fig. 5. Cavern A has a hypothetical regular shape with smooth curvatures and no sharp angles. On the other hand, cavern B is meant to reproduce a more realistic scenario, where a complex geometry wider at the bottom and narrower towards the top is adopted. For the sake of comparison, both caverns have the same volume and height.

The impact of a non-salt layer intercepting the cavern is investigated using cavern B. It can be noticed in Fig. 5, that cavern B has a region that can represent a non-salt layer or salt, depending on the material parameters adopted.

4.3. Boundary conditions

The boundary conditions applied to the geometries are depicted in Fig. 6. The overburden is included by imposing a load of 10 MPa on the top boundary. The two vertical plane boundaries not in contact with the cavern are subjected to a side burden following the lithostatic pressure with $\rho_{\mathrm{salt}} = 2000\ \mathrm{kg/m^3}$. The other two vertical plane boundaries are prevented from normal displacement. The gas pressure is imposed as a uniform pressure distribution on the cavern walls, and the cavern pressure schedules are shown in Fig. 6. Pressure schedules S1 and S2 start from 13 MPa followed by 2 h of production, during which the cavern pressure drops by 1 MPa and 5 MPa, respectively. Compared to S2, the pressure schedule S1 is expected to cause smaller stresses on the cavern walls. Both schedules S1 and S2 have a short duration of 24 h. On the other hand, the pressure schedule S3, shown below, represents a more realistic case in which fast and irregular cyclic operation is imposed for approximately 40 days.

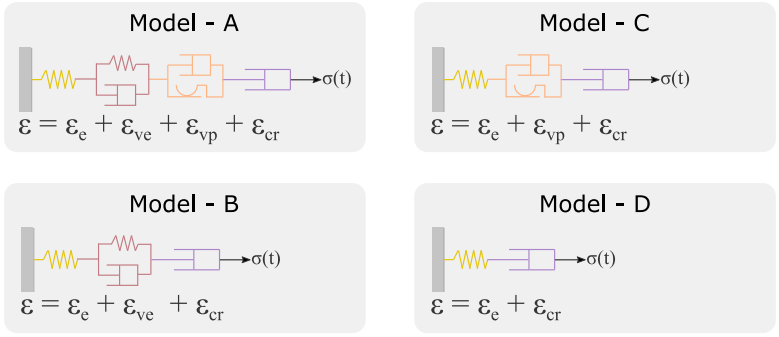

Fig. 4. Constitutive models A (elastic, viscoelastic, viscoplastic and dislocation creep), B (elastic, viscoelastic and dislocation creep), C (elastic, viscoplastic and dislocation creep), and D (elastic and dislocation creep).

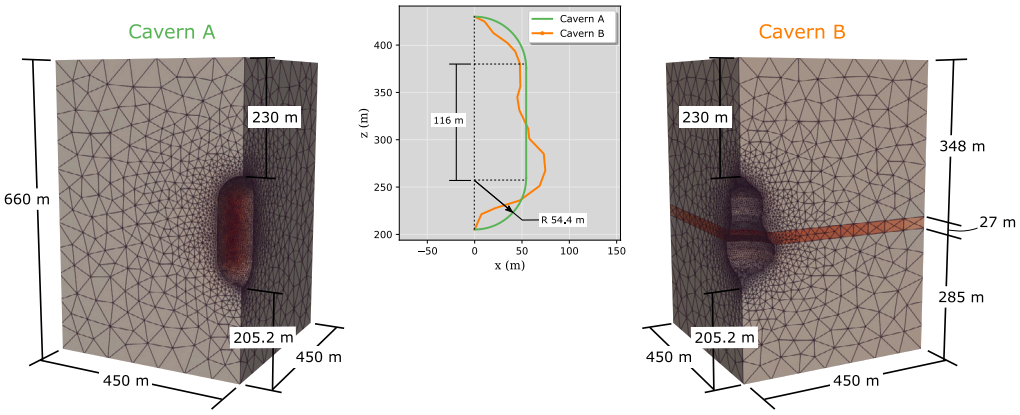

Fig. 5. Single cavern geometries with different cavern shapes (A and B).

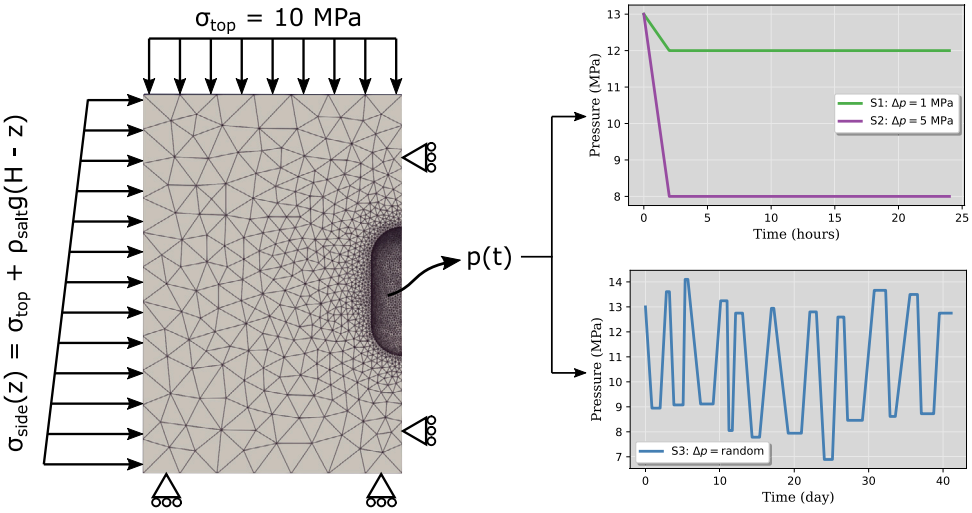

Fig. 6. Boundary conditions and pressure schedules (i.e., operational fluctuating pressure values) for regular depletion (top-right) and random cyclic (bottom-right) scenarios.

In addition to single cavern simulations, we also investigate the mechanical behavior of systems of caverns. In this work, we consider the caverns to be equally spaced from each other and placed in alternate positions as shown in Fig. 7. The symmetries associated with this configuration allow for the simulation of only a small portion of the system, in a similar manner as the well-known five-spot problem for reservoir simulations. All vertical planar boundaries are prevented from normal displacement. Additionally, the chosen distances between the caverns (pillar width) are $L = 0.5R$, $L = 1R$, $L = 2R$ and $L = 10R$, as shown in Fig. 7. The pressure schedules imposed on Caverns 1 and 2 are illustrated in Fig. 8. As shown in this figure, R is the characteristic radius of the caverns. Although this five-spot configuration is an idealized situation, thus preventing the results from being extrapolated to real systems of caverns, it provides the necessary ingredients to analyze how the interactions between adjacent caverns take place.

4.4. Initial condition

The initial condition is computed by solving an equilibrium problem before the pressure schedule is applied. In the equilibrium stage, a

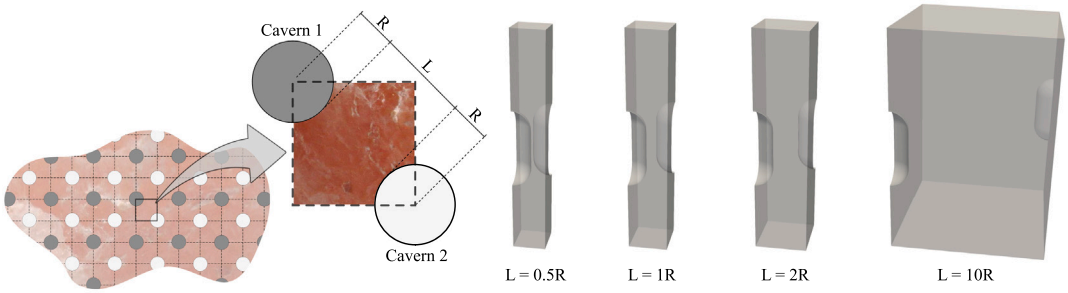

Fig. 7. System of caverns configuration and geometries employed.

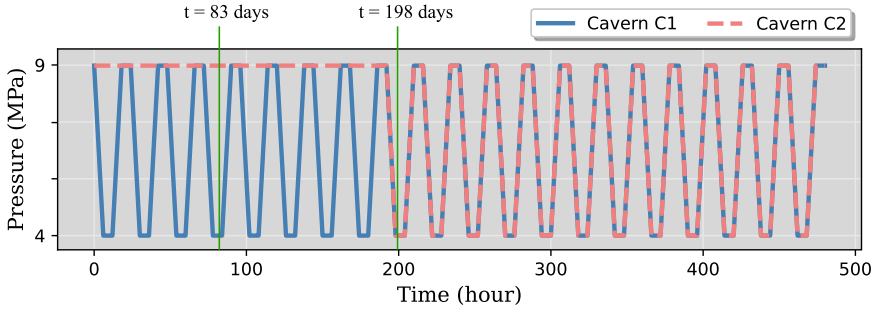

Fig. 8. Pressure schedule S4 imposed to caverns 1 and 2, shown in Fig. 7.

constant pressure of $p(t=0) = 13$ MPa (for all S1, S2 and S3 scenarios) with the boundary conditions as illustrated in Fig. 6 until the steady-state (equilibrium) condition is reached. In addition, only the elastic and viscoelastic elements are considered for the equilibrium condition. By the end of this stage, the equilibrium viscoelastic strain and strain rate are assigned to the initial conditions of the operation stage, where the pressure schedule is imposed on the cavern. The initial strain and strain rates are considered zero for the inelastic elements.

After the equilibrium state is obtained, the resulting stress condition on every element is considered to be located at the onset of viscoplasticity, i.e., on the yield surface. Therefore, any additional load applied to the cavern will cause viscoplastic deformation. This is ensured by manipulating Eq. (6) with $F_{vp}(\boldsymbol{\sigma}, \alpha_0) = 0$ and solving for the initial hardening parameter, i.e.,

$$\alpha_0 = \gamma I_1^{2-n} - \frac{J_2}{I_1^n}\left(\exp\left(\beta_1 I_1\right) + \beta\cos\left(3\theta\right)\right). \tag{33}$$

4.5. Factor of safety

The Factor of Safety (FOS) is a practical quantity often used to assess the likelihood of tertiary creep to occur [42]. It is defined as

$$\text{FOS} = \frac{\sqrt{F_{\text{dil}}(\boldsymbol{\sigma})}}{\sqrt{J_2}}, \tag{34}$$

where $F_{\text{dil}}(\boldsymbol{\sigma})$ describes the compressibility/dilatancy boundary according to Desai's [43] model, and it is given by

$$F_{\text{dil}}(\boldsymbol{\sigma}) = \left(1 - \frac{2}{n}\right)\gamma I_1^2\left[\exp\left(\beta_1 I_1\right) - \beta\cos\left(3\theta\right)\right]. \tag{35}$$

Tertiary creep is expected to occur when FOS$\leq$ 1.0.

4.6. Laboratory experiment

The laboratory experiment used in this paper consists of a triaxial test on a salt sample, where the axial stress is applied cyclically and the confining pressure (radial stress) is kept at a constant level. The stress conditions and the axial and radial strain measured during the experiment are shown in Fig. 9. The details of the experimental setup can be found in [50].

4.7. Material parameters

For model calibration purposes, the material parameters are divided into three groups. The first group comprises the parameters associated with the elastic and viscoelastic elements, which are calibrated from the unloading/reloading cycles. The second group comprises the dislocation creep element, whose parameters are defined by matching the strain rates observed at the end of each loading cycle. Finally, the parameters β, m, n_1, γ and σ_t are taken from the literature [43,61], while the rest is manually calibrated in this work. Further details on the calibration procedure can be found in [50]. Table 1 shows two material parameter sets for the constitutive model: Salt-A and Salt-B. As discussed in [50], many possible material parameter sets can fit one single experiment, which is the reason Salt-A and Salt-B are equally acceptable in the absence of additional laboratory experiments. These two parameter sets were obtained by manually fitting the constitutive model against the laboratory experiment described in Section 4.6.

Table 1 also presents the material parameters for Anhydrite and Mudstone, which will be used as interlayers for Cavern B (see Fig. 5). These two materials are assumed to be purely elastic, with no time-dependent behavior. The elastic properties of anhydrite and mudstone are taken from [49,66], respectively.

4.8. Code implementation

The three-dimensional salt cavern simulator is developed using Python language. The weak formulation presented in Section 3 is solved by finite elements using Dolfin [67], from FEniCS project version 2019.1 [68]. The geometries and meshes are created in Gmsh [69] version 4.10.1 and subsequently converted to .xml format using dolfin-convert command. Regarding time integration, the Crank–Nicolson ($\theta = 0.5$) is employed most of the time, except when the time step sizes are required to be too small, in which case the explicit formulation ($\theta = 1.0$) is adopted. Finally, the resulting linear systems are solved using PETSc [70] implementation of the conjugate gradient (CG) method and the successive over-relaxation (SOR) as a preconditioner. The simulator is fully open-source, and it is available at our Gitlab repository.

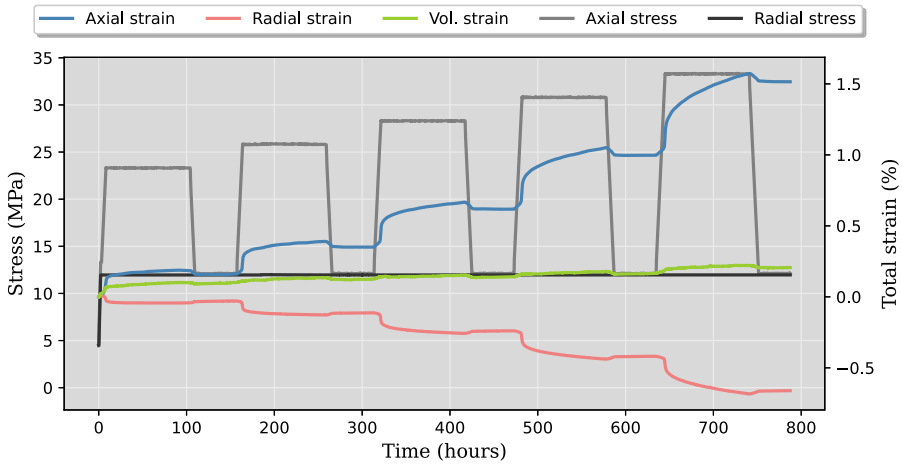

Fig. 9. Experimental results obtained from a cyclic loading triaxial test.
Source: Extracted from [50].

Table 1
Sets of material properties for halite (Salt-A, Salt-B), anhydrite and mudstone.

Element	Property	Units	Salt-A	Salt-B	Anhydrite	Mudstone
Elastic	E_0	GPa	79	118	61.5	19.33
	ν_0	–	0.32	0.32	0.32	0.223
Viscoelastic	E_1	GPa	45	42	–	–
	ν_1	–	0.32	0.32	–	–
	η_1	Pa s	3.7e14	2.5e14	–	–
	μ_1	s^{-1}	1e−12	6.65e−13	–	–
	N_1	–	3.053	3.053	–	–
Viscoplastic	a_1	MPa^{2-n}	1.3e−05	2e−05	–	–
	η	–	0.827	0.8	–	–
	β_1	MPa^{-1}	0.004459	0.001011	–	–
	β	–	0.995	0.995	–	–
	m	–	−0.5	−0.5	–	–
	n_1	–	3.0	3.0	–	–
	γ	–	0.088012	0.088012	–	–
	σ_t	MPa	5.4	5.4	–	–
Dislocation creep	A	$Pa^{-n}\ s^{-1}$	5.9e−29	1.1e−21	–	–
	n	–	4.0	3.0	–	–
	T	K	298	298	–	–
	Q	J/mol	51 600	51 600	–	–
	R	$J\ K^{-1}\ mol^{-1}$	8.32	8.32	–	–

4.9. Model assumptions

In simulations conducted in this study, a few important hypotheses are assumed. The first one is the small strain assumption (Eq. (32)), which is one of the reasons we simulate relatively short periods of operation (around 40 days). For such a short period, pressure solution creep is also neglected from the constitutive model. The in-situ rock is at a homogeneous temperature of 298 K, which is the same temperature as the injected gas, so the whole process is isothermal. Finally, rock salt is always assumed to be homogeneous, which is hardly the case for real applications but it serves the purposes of the present investigation.

5. Simulation results

The numerical analyses conducted in this work are presented in this section. The finite element implementation (i.e. "SafeInCave" simulator) is first verified against the material point method, as explained below. In the sequence, the sensitivity analyses of salt cavern deformations and stress states are carried out, as discussed in Section 4.

5.1. Verification

Before proceeding with the sensitivity analyses, it is important to verify the correct implementation of the constitutive model into the finite element (FEM) simulator. For this purpose, a 1 m cubic salt rock sample (Ω) is subjected to the triaxial loading condition shown in Fig. 10-a. Because of the cubic shape of the salt sample and the homogeneous compressive stresses applied to its boundaries, the stress distribution is homogeneous inside the domain (and so are the deformations), and it is given by

$$\boldsymbol{\sigma}(\mathbf{x},t) = \begin{bmatrix} \sigma_{\mathrm{h}}(t) & 0 & 0 \\ 0 & \sigma_{\mathrm{h}}(t) & 0 \\ 0 & 0 & \sigma_{\mathrm{v}}(t) \end{bmatrix} \quad \forall \ \mathbf{x} \in \Omega, \tag{36}$$

where $\sigma_{\mathrm{v}}(t)$ and $\sigma_{\mathrm{h}}(t)$ denote the normal compressive stresses applied in the vertical and horizontal directions, respectively. Note that a triaxial stress condition does not induce shear stresses, hence the off-diagonal zeros. Since the stress tensor is known, the contributions of each element in the constitutive model (Fig. 2) to the total strain tensor can be calculated using the material point method (MP), as presented in Appendix. By contrast, the finite element solution does not assume the stresses are known inside the domain. Instead, the stress tensor on each grid element is calculated during the simulation, which makes these two approaches fundamentally different even though the solution is the same.

Fig. 10-b compares the vertical (ε_v) and horizontal (ε_h) strains obtained with the finite element simulator (FEM) and the material point method (MP). It is shown that both solutions are in good agreement.

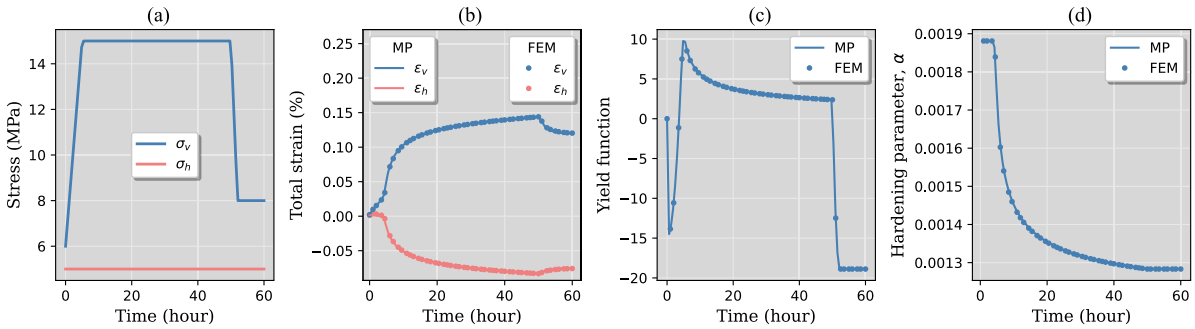

Fig. 10. (a) Loading conditions; (b) Total strains, (c) yield function values, and (d) hardening parameter values obtained with the finite element (FEM) and material point (MP) methods.

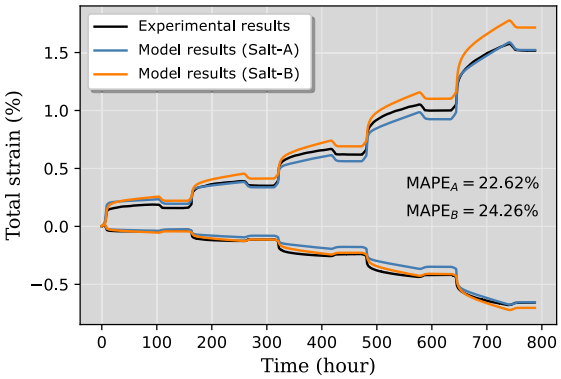

Fig. 11. Model calibrations against experiments A and B. Quantities MAPE$_A$ and MAPE$_B$ represent the mean absolute percentage error for parameter sets Salt-A and Salt-B, respectively.

Moreover, Figs. 10-c and 10-d respectively show yield function and hardening parameter (α) values calculated during the simulation for the two approaches. The results presented in Fig. 10 confirm the correct implementation of the constitutive model in the finite element simulator.

5.2. Influence of model calibration

In this subsection, we investigate the impact of model calibration on describing laboratory experiments and salt cavern simulations. As discussed in Section 1, the complex mechanical behavior of salt rocks often leads to constitutive models that depend on many parameters, which renders the calibration challenging. For instance, the creep element requires that salt samples reach steady-state creep to properly define the power law coefficients. However, it is not possible to ensure the experiment shown in Fig. 9 actually reaches this condition. Additionally, the viscoplastic element requires at least six experiments specifically designed to determine its material parameters. The elastic and viscoelastic properties are also challenging to be unambiguously defined. Consequently, there might be many combinations of material parameters that can fit a single laboratory experiment [50]. The set of parameters Salt-A and Salt-B, shown in Table 1, were chosen to expose this particular issue. As shown in Fig. 11, both parameter sets provide reasonably good description of the experimental results, with a mean absolute percentage error (MAPE) of 22.62% and 24.26% for Salt-A and Salt-B, respectively.

The fact that parameters Salt-A and Salt-B provide similar results in laboratory experiments could suggest that running a salt cavern simulation with either of them would also produce similar results. To investigate this hypothesis, salt cavern simulations are performed considering both material parameter set: Salt-A and Salt-B. In this case, the Cavern A of Fig. 5 is employed and the pressure schedule S3 (Fig. 6) is imposed on the cavern walls. The volume loss of the cavern is monitored over time and the results are presented in Fig. 12. After 40 days of operation, the difference between the two simulations is substantial. Two linear equations, $C_A(t)$ and $C_B(t)$, are fitted against both solutions using least-squares. Using these equations to predict the cavern convergence after 100 years of operation provide around 28% and 68% for Salt-A and Salt-B, respectively. This is a significant difference of results and it emphasizes the importance of model calibration for salt cavern simulations.

5.3. Importance of deformation mechanisms

As discussed before, the constitutive model adopted in this work includes different deformation mechanisms to describe the mechanical behavior of salt rocks. The elastic component is intended to capture the instantaneous elastic material response. Reverse creep, on the other hand, is often described as a time-dependent deformation response that follows an unloading phase. In the stress–strain graph, this phenomenon manifests a hysteretic curve during unloading and reloading paths. It is well-known that viscoelastic materials present this behavior, which is why a Kelvin–Voigt element is included in the constitutive model. Transient creep is intended to be captured by the viscoplastic model, as presented in Section 2. Finally, dislocation creep is described by a well-established power law function. For hydrogen operations, the loading conditions are expected to constantly change during the cavern's life cycle, thus suggesting that transient and reverse creep might always be present. The constitutive models presented in Section 4.1 are employed to investigate the importance of each deformation mechanism in laboratory experiments and salt cavern simulations. The set of material parameters used in models A to D is the one of Salt-A, summarized in Table 1. Therefore, the elastic and dislocation creep parameters are the same for all models; the viscoelastic parameters are the same for models A and B; and the viscoplastic parameters are the same for models A and C.

Fig. 13 shows the first 175 h of experiment A (see Section 4.6) and the fitting results obtained with models A, B, C and D (see Section 4.1). It can be noticed that models B and D provide relatively good results during the first loading step (i.e. from 0 to 100 h), but most of the deformation is recovered during the unloading step, which does not agree with the experimental results. The right graph of Fig. 13 shows that the stress–strain curves obtained with these two models are completely different from the experimental data. Conversely, the inclusion of the viscoplastic element allows for models A and C to correctly describe both loading and unloading stages. However, when the stress–strain curve is considered, model C is not able to capture the reverse creep characterized by the hysteretic path observed during unloading/loading steps.

The same models presented in Section 4.1 are now employed to solve the salt cavern problem. For this test case, the pressure schedules

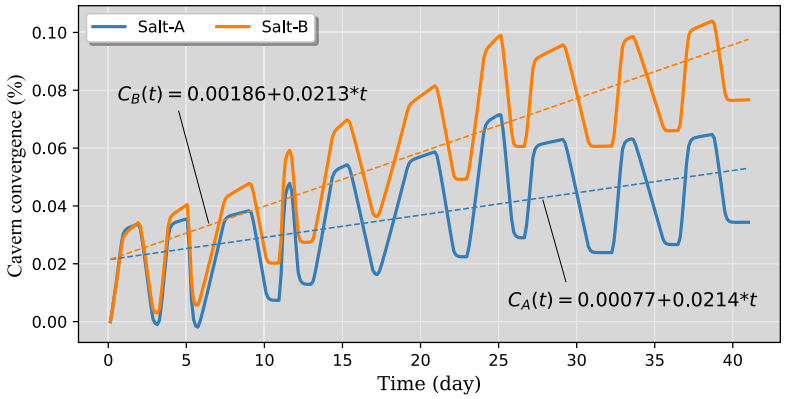

Fig. 12. Cavern convergence obtained with Salt-A and Salt-B parameter sets.

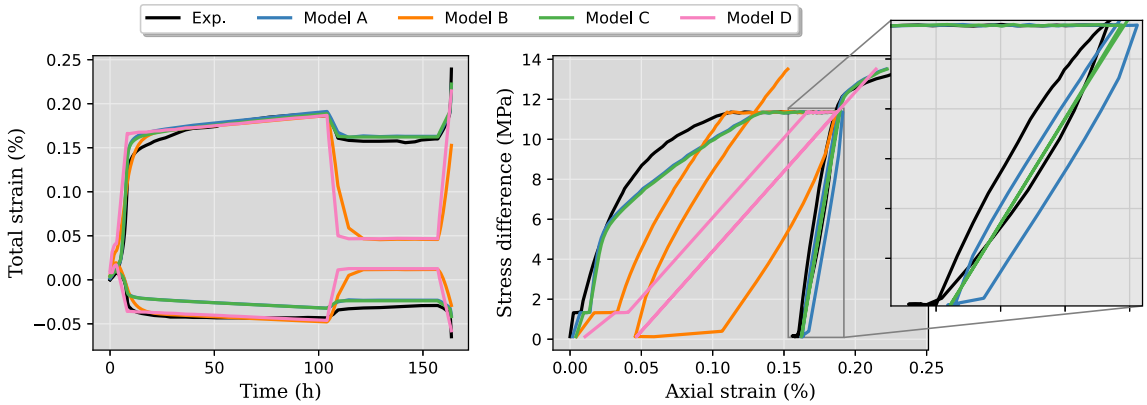

Fig. 13. Results obtained with different constitutive models to describe experiment A. The models A, B, C, and D are illustrated in Fig. 4.

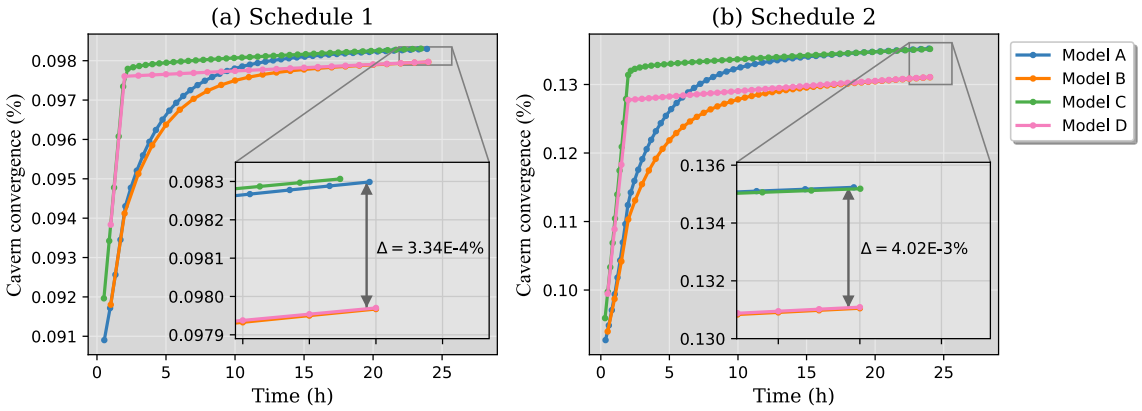

Fig. 14. Cavern convergence obtained with different constitutive models considering pressure schedules S1 (a) and S2 (b). The models A, B, C, and D are illustrated in Fig. 4.

S1 and S2 (see Fig. 6) are imposed on the walls of cavern A in Fig. 5. The results presented in Fig. 14-a show a small difference between models A and B, suggesting that viscoplasticity does not make much difference. However, a significant difference between models A and C (and also between B and D) is observed, which is due to the presence or not of the viscoelastic element. For the pressure schedule S2, shown in Fig. 14-b, the viscoplastic contribution during gas production is increased by one order of magnitude, which can be verified by the difference between models A and B and between models C and D. The same observations regarding the viscoelastic contribution for pressure schedule S1 also hold for S2. It should be stressed, however, that both schedules S1 and S2 are inducing viscoplasticity because gas pressure is being depleted below the historical minimum, which is 13 MPa in this case. When the gas pressure increases again, additional viscoplasticity will occur only in the next production period if gas pressure drops below the minimum historical pressures (i.e. 12 MPa for S1 and 8 MPa for S2).

The results presented in Fig. 14 suggest that the difference between models A and B (or C and D) is expected to grow with time only if the minimum historical pressure is exceeded in the future, which would trigger additional viscoplastic deformation. This situation is reproduced in pressure schedule S3, where the minimum gas pressure is often exceeded during the operation (see Fig. 6). To investigate this hypothesis, the pressure schedule S3 is imposed on Cavern A (Fig. 5) and the results are shown in Fig. 15 for models A, B, C and D. As observed before in Fig. 14, model A provides similar results as model

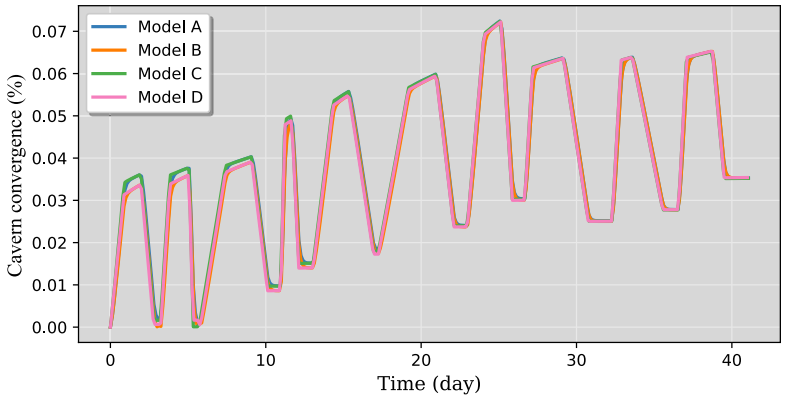

Fig. 15. Cavern convergence obtained with different constitutive models considering pressure schedule S3.

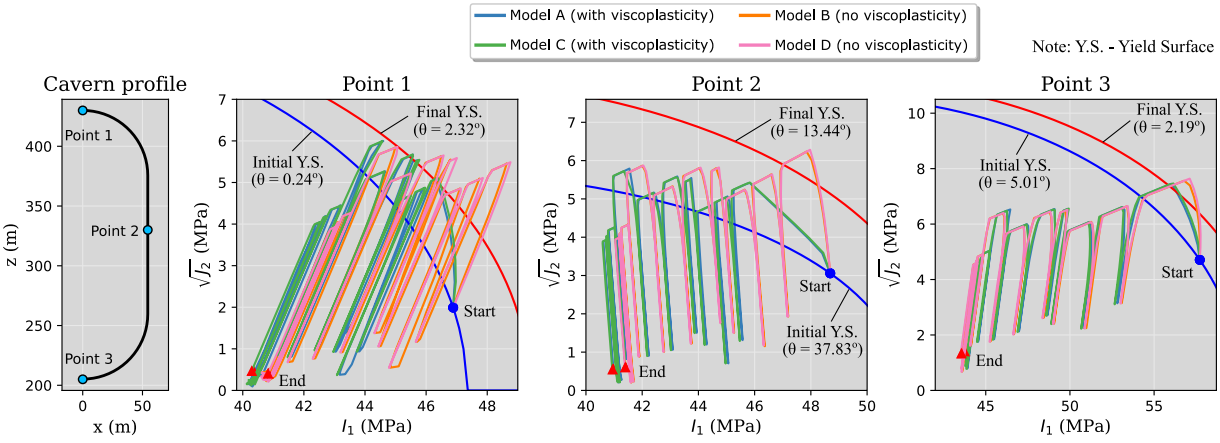

Fig. 16. Stress paths at different positions of the cavern wall obtained with models A, B, C and D. The figures show the start (blue circles) and end (red triangles) points for all stress paths. The initial and final yield surfaces are also shown (note the different Lode's angle, θ, for each case).

C (the same holds for models B and D), which is directly linked with the presence of the viscoplastic element. During the first three to five cycles, the two models that include the viscoplastic element (models A and C) predict higher cavern convergence than models B and D, which neglect viscoplasticity. Interestingly, this difference tends to vanish as the operation progresses and all models predict virtually the same cavern convergence.

The results shown in Fig. 15 are somewhat surprising as the initial differences due to the presence of viscoplasticity tend to vanish towards the end of the simulations. To further investigate this phenomenon, the stress paths produced by each model are analyzed at different positions of the cavern. Fig. 16 shows the stress paths at the top (point 1), middle (point 2), and bottom (point 3) of the cavern wall. Regardless of the model, all points start from the same stress state but finish at slightly different positions. It is shown that the presence of the Kelvin–Voigt element (viscoelasticity) does not produce significant stress differences, as similar results are obtained with models A-C and B-D. On the other hand, the presence of a viscoplastic element does change the stress paths, particularly during the first pressure drop inside the cavern. Fig. 16 also shows the initial and final yield surfaces for all three points. It can be verified that the three initial yield surfaces are crossed as soon as the cavern pressure starts to decrease, thus inducing viscoplastic deformation. However, the stress paths tend to move to the left (towards lower mean stresses), so additional viscoplasticity does not necessarily occur, even though the minimum gas pressure is exceeded a few times during the operation. This shows the complexity of the stress behavior around the cavern walls. Finally, it should be noted that the comparison between the initial and final position of yield surfaces must be done keeping in mind the value of the Lode's angle, θ (see Eq. (6)). This is the reason, for example, that the final yield surface of point 2 seems to be disconnected from the stress path.[3]

An important observation of Fig. 16 is that different stress paths are obtained depending on whether or not the viscoplastic element is considered in the constitutive model. This means that the dislocation creep element, which is present in all four models, perceives different stresses, thus resulting in different dislocation creep strain rates. If the average Von Mises stresses (considering the entire simulation) perceived by models B and D are higher than those perceived by models A and C, then the dislocation creep rates for models B and D would be higher than those for models A and C. In this manner, the higher cavern convergence observed for models A and C at the beginning of the simulation (see Fig. 14) would be compensated by higher dislocation creep rates of models B and D, thus explaining the solutions of all four models converging to each other towards the end of the simulation. To test this hypothesis, a simultaneous temporal and spatial average of the Von Mises stress is calculated as

$$\bar{q} = \frac{1}{N_t N_e} \sum_{j=1}^{N_t} \sum_{i=1}^{N_e} q(\mathbf{x}_i, t_j), \tag{37}$$

where N_t and N_e denote the number of time steps of the simulation and the number of elements of the grid, respectively. Additionally, $q(\mathbf{x}_i, t_j)$ represents the Von Mises stress at position $\mathbf{x}_i$ and time t_j. A comparison of the average Von Mises stress for the four models is presented in Table 2. It shows that $\bar{q}$ is indeed bigger for models B and

[3] It can be seen that the stress paths of points 1 and 3 are touching their corresponding final yield surfaces, but this is not the case for point 2.

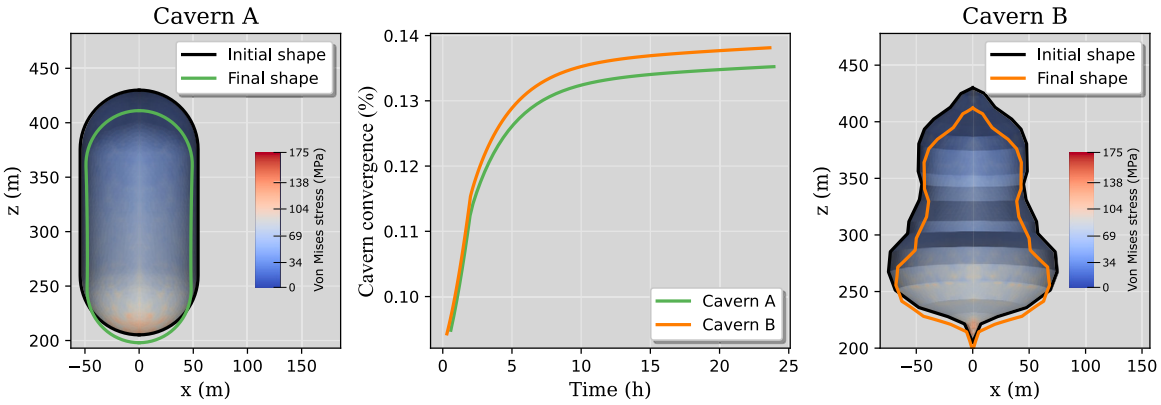

Fig. 17. Initial and final shape of caverns A and B on the left and right, respectively (displacements are amplified 200 times for visualization). In the middle, cavern convergence over time for both caverns.

Table 2
Average Von Mises stress.

Model	A	B	C	D
$\bar{q}$ (MPa)	3.46	3.56	3.44	3.55

D, suggesting that these models undergo slightly higher stresses and, therefore, produce larger dislocation creep rates than models A and C.

The results shown in this section seem to suggest that including transient creep in the constitutive model is not important. However, the analysis performed in the present study is not enough to extend this conclusion beyond the models adopted in this work. In other words, other models found in the literature could produce different results depending on whether or not transient creep is included. Moreover, although Fig. 15 indicates that the cavern convergence is not affected by the inclusion of transient creep in the long-term, Fig. 16 shows that the stresses are significantly altered, which would be important, for example, to predict tertiary creep (i.e. mechanical stability).

5.4. Impact of cavern shape

During cavern construction, the leaching process of the salt rock results in caverns with irregular and complex shapes. The presence of sharp angles on the cavern walls can create regions of stress concentration which induce higher creep rates and, potentially, tertiary creep. To study this case, we first compare the behavior of Cavern A (regular shape) and Cavern B (irregular shape) under the pressure schedule S2 (see Fig. 6). The results are presented in Fig. 17, which shows the initial and final shape of both caverns and the cavern convergence over time. The left and right graphs also show the von Mises stresses on the cavern walls by the end of the simulation. Although it is not possible to visually identify regions of stress concentrations in Cavern B, the graph in the middle shows a higher volume loss for this cavern when compared to Cavern A. Interestingly, the difference between the two curves is observed to increase right after the production phase, that is, after the first 2 h. This is attributed to slightly higher stresses that increase strain rates.

The possibility of tertiary creep is investigated by analyzing the factor of safety (FOS), as defined in Section 4.5. The factor of safety is computed by post-processing the stress field at each element of the grid. In the sequence, we sum up the volumes of all the elements where FOS$\leq$ 1.0 and divide by the total volume of the entire geometry. This gives the volumetric percentage of elements undergoing tertiary creep, and the results are presented in Fig. 18. By the end of the production period, the volume of salt undergoing tertiary creep (FOS$\leq$ 1.0) is bigger for Cavern B than for Cavern A, which is a consequence of the higher stress concentration regions. Moreover, in both cases, the volume of elements with FOS$\leq$ 1.0 decreases over time due to stress relaxation, but the rate of decay is higher for Cavern B. This seems to suggest that irregular cavern shapes initially induce higher stresses, thus causing more cavern convergence and tertiary creep, but it also favors stress redistribution. Fig. 18 also shows the elements with FOS$\leq$ 1.0 for both caverns at two different times. Most of these elements are located at the bottom of the caverns, but a few elements also appear at the top of Cavern B.

5.5. Impact of interlayers (heterogeneity)

Although homogeneous distributions of halite can be found in the center of salt domes, the lithology of bedded salt formations can become considerably more complex, with the presence of different types of insoluble interlayers such as anhydrite, gypsum, mudstone, etc [37,49,71]. In this section, we study the impact of the presence of anhydrite and mudstone interlayers on the volume loss of a cavern operating under the pressure schedule S3 (see Fig. 6). For comparison, this problem is solved with three different property distributions: (i) a homogeneous distribution of halite (Salt-A in Table 1) in the entire domain; and halite (Salt-A) with an interlayer of (ii) mudstone and (iii) anhydrite crossing the Cavern B of Fig. 5. Both anhydrite and mudstone are assumed to be purely elastic with the properties shown in Table 1. Fig. 19 shows the cavern convergence obtained for the three cases. Because mudstone is softer (lower Young's modulus) than halite, the amplitude of the cavern convergence oscillations with the mudstone interlayer case is slightly bigger than that without interlayer. The fact that the mudstone layer is not considered to undergo creep contributes to reduce cavern convergence when compared to the purely halite distribution. Conversely, the amplitude of oscillations for the anhydrite interlayer case is smaller than the other cases due to its higher stiffness. The presence of an anhydrite layer is also shown to inhibit cavern convergence even more than in the mudstone case.

The difference between the three curves in Fig. 19 after 40 days of operation is not significant. In order to predict the difference between these solutions in the long term, linear equations are fitted using least squares, resulting in equations $C_{an}(t)$, $C_{mu}(t)$ and $C_{ni}(t)$ for the cases with anhydrite interlayer, mudstone interlayer and with no interlayer, respectively. Assuming the loading conditions remain approximately the same as in pressure schedule S3 for the next 100 years, these three equations predict volume losses of 19.2%, 23.2% and 28.1% for anhydrite, mudstone and no interlayer, respectively. In other words, the differences between cavern convergences obtained by considering or not the interlayers after 100 years of operation are approximately 5% for the mudstone interlayer and 9% for the anhydrite interlayer when compared to the no interlayer case.

Although these results suggest that the presence of an interlayer has little impact on cavern convergence, this should not be readily extrapolated to real applications. Even salt domes, in which homogeneous

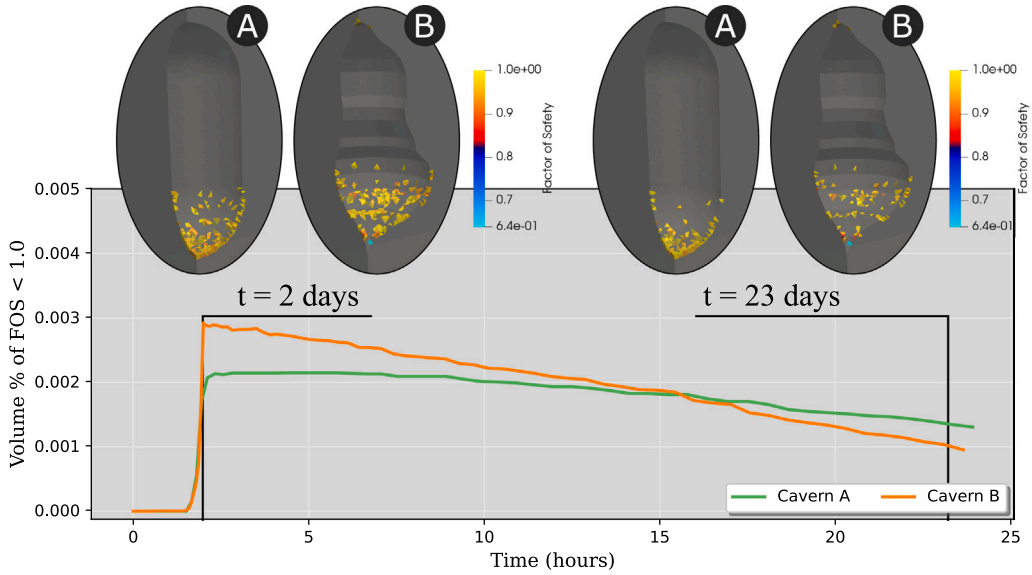

Fig. 18. Percentage of salt rock volume undergoing tertiary creep (FOS≤ 1.0).

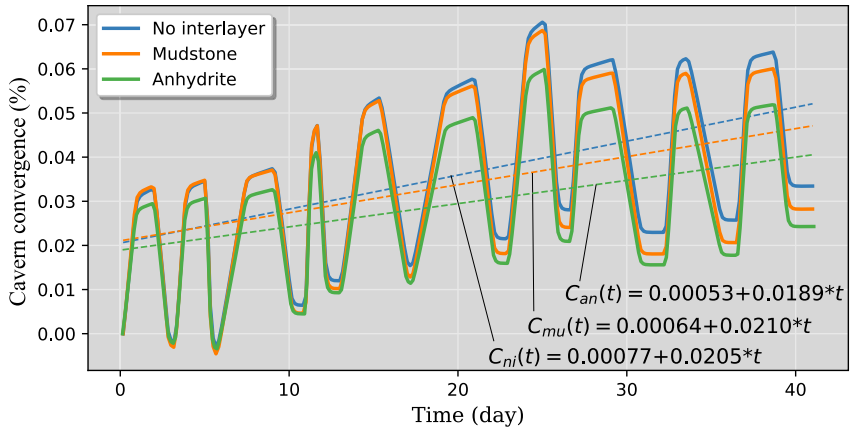

Fig. 19. Cavern convergence obtained with no interlayer, mudstone interlayer and anhydrite interlayer. Fitted equations $C_{an}(t)$, $C_{mu}(t)$ and $C_{ni}(t)$ consider time in days.

regions of halite are more likely to be observed, often present stringers with many different compositions [72] not just in the flanks, but also in the central portions. Bedded formations tend to present simpler structures but are usually composed of many interlayers. Therefore, the mechanical response of salt caverns can be significantly impacted by the presence of such complex heterogeneity patterns. Nevertheless, the results presented in Fig. 19 provide a sense of how much impact a simple heterogeneous structure can have on the cavern deformations.

5.6. System of caverns

To investigate the mechanical stability of a system of caverns, the geometries illustrated in Fig. 7 are considered and the cavern convergence and FOS for each configuration are analyzed. The pressure schedules applied to the caverns are illustrated in Fig. 8, which shows that Cavern 2 is kept at a constant pressure of 9 MPa for 192 h, whereas a cyclic loading is imposed on Cavern 1 during the entire simulation. After 192 h, Cavern 2 is also subjected to the same cyclic loading in synchronicity with Cavern 1. In this manner, it is possible to study how the operation of one cavern affects the operation of the other.

Fig. 20 shows the cavern convergence results of both caverns for the 4 cavern configurations. For the case where $L = 0.5R$, it is possible to notice some oscillations in Cavern 2 due to the operations in Cavern 1 during the inactive period of the former. These oscillations are not observed for the other cases and are attributed to the excessive proximity between the two caverns. Another interesting fact is that the cavern convergence rate increases after Cavern 2 starts to operate, which can be observed in both $L = 0.5R$ and $L = 1R$ but not for larger pillar widths. Moreover, although mutual interaction does not seem to take place for $L = 2R$, it is possible to notice that after 20 days the cavern convergence for this case is larger than for $L = 10R$. This is related to the narrower pillar width available to sustain the overburden, resulting in higher stresses and thus higher cavern convergence. It is important to point out that the results shown in Fig. 20 are in agreement with [55], which establishes that the minimum allowable pillar width should be between 2 to 2.5 times the cavern diameter.

The stress fields obtained are used to compute the factor of safety (FOS), as described in Section 4.5, for each element of the grid. The results are shown in Fig. 21 for when only Cavern 1 is operating ($t = 83$ days) and for when both caverns are in operation ($t = 198$ days). Times $t = 83$ days and $t = 192$ days are indicated in Fig. 8. The red elements indicate where tertiary creep is most likely to occur (FOS≤ 1.0). For $t = 83$ days, a clear interaction between the two caverns is observed for $L = 0.5R$ and $L = 1R$, but Cavern 2 is not significantly affected for $L = 2R$ and $L = 10R$. When Cavern 2 is also in operation, the elements with FOS≤ 1.0 meet in the middle of the two caverns, indicating mutual

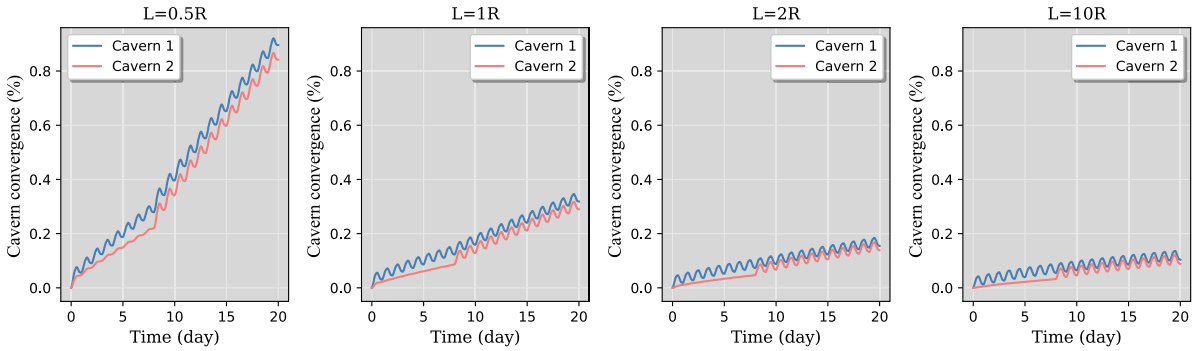

Fig. 20. Cavern convergence for the systems of caverns considering different distances between neighbor caverns.

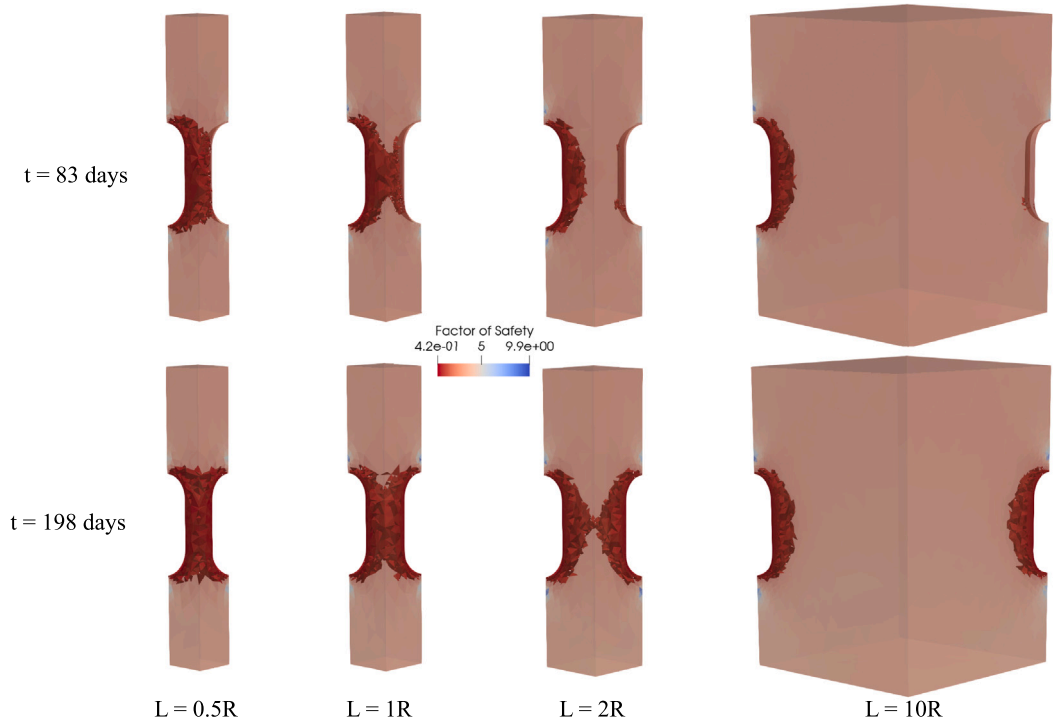

Fig. 21. Factor of safety distribution highlighting in red the elements with high probability of presenting tertiary creep (FOS≤ 1.0).

interaction for $L = 2R$. Although tertiary creep is induced in both caverns during the double cyclic operation period, mutual interaction is not observed for $L = 10R$.

6. Conclusions

This work presented 3D simulation and sensitivity analyses of salt caverns for energy storage, with particular attention devoted to cyclic loading conditions. A comprehensive constitutive model composed of elastic, viscoelastic, viscoplastic and dislocation creep was proposed. The finite element method was employed to solve the non-linear set of equations on unstructured grids. The formulation allows for different time integration schemes (explicit, Crank–Nicolson and fully-implicit) to be used. Sensitivity analyses were performed to investigate key parameters with high impact on salt cavern simulations. The analyses aimed to investigate the influence of model calibration, different deformation mechanisms, the impact of cavern geometry and non-salt interlayers, and mutual interactions in systems of caverns. The main conclusions are summarized below:

- Model calibration should be carefully performed to avoid misleading simulation results. For complex constitutive models, there might be different sets of material parameters that present a reasonably good fit against laboratory experiments but lead to very different performance analyses at the salt-cavern scale.
- Viscoplastic deformation, describing transient creep, was found crucial in reproducing the laboratory experiments on rock salt specimens (cm-scale). However, for the cases studied in this work, the results suggest that viscoplasticity does not play a crucial role in cavern-scale deformation simulations under cyclic loading. Nevertheless, the stress path is significantly affected by viscoplasticity. It must be emphasized that this remark is valid for the specific constitutive model employed in this work. Although other constitutive models might lead to different conclusions, it is hard (if not impossible) to tell which one is correct, since it is not possible to identify the different deformation mechanisms from field measurements (e.g. sonar cavity measurements).
- After a pressure drawdown (or build-up) stage, the viscoelastic deformations (i.e. reverse creep) is important for a relatively short period of time, i.e., approximately 10 h. After this period, the effects of reverse creep vanish and no cumulative impacts are observed in the long-term.

- Irregular cavern shapes do not necessarily induce more volume loss, but they can increase the likelihood of tertiary creep to occur. Interestingly, sharp angles are shown to favor a faster stress redistribution, thus abbreviating the period of tertiary creep. In other words, cavern shapes with sharp angles induce more tertiary creep, but for a shorter period. Nevertheless, caverns with sharp angles should be avoided in order to prevent tertiary creep from occurring.
- Although the presence of interlayers has an impact on the simulation results, the influence is not as significant as the model calibration. Moreover, it was observed that stiffer interlayers decrease the speed of cavern volumetric closure.
- By analyzing the factor of safety, mutual interaction between neighboring caverns can be observed for pillar width less than 2 times the cavern radius. Therefore, larger distances should be considered when designing safe systems of caverns for large-scale energy storage.

One of the main contributions of this work was to perform sensitivity analyses to identify important parameters that affect salt cavern simulations. However, as with any underground activity, energy storage in salt caverns is full of uncertainties and much work is yet to be done. Future studies need to consider geological uncertainties, such as heterogeneity distributions, by the use of e.g. Monte Carlo simulations and data assimilation techniques. It is also worth mentioning that artificial intelligence can be found effective in material characterization, once enough reliable data sets are available. Finally, the mechanical behavior of salt caverns after abandonment is currently a matter of concern by regulation authorities and therefore deserves attention from the scientific community. Processes such as pressure solution creep and thermal strains, not considered in the present study, might have a significant impact in these situations.

CRediT authorship contribution statement

Hermínio T. Honório: Writing – original draft, Visualization, Validation, Software, Methodology, Formal analysis, Conceptualization. **Hadi Hajibeygi:** Writing – review & editing, Methodology, Conceptualization.

Declaration of competing interest

The authors declare that they have no known competing financial interests or personal relationships that could have appeared to influence the work reported in this paper.

Acknowledgments

This research was partly supported by Shell Global Solutions International B.V. within the project “SafeInCave”. The developments of this study have been made in an open-source “SafeInCave” simulator, which can be found in our Gitlab repository. The authors also acknowledge members of the ADMIRE and DARSim research groups at TU Delft for the fruitful discussions during the development of this work. Additionally, the authors acknowledge the fruitful discussions with the staff of Shell Global Solutions International B.V., namely, Dr. Maartje Houben, Dr. Kevin Bisdom, Dr. Thomas Fournier, and Dr. Karin de Borst. Also, fruitful discussions with Prof.dr.ir. Lambertus Sluys of TU Delft are acknowledged.

Appendix. Material point method

The material point method can be used when the stress tensor is known, which is the case for triaxial tests performed in cubic or cylindric samples. For the constitutive model employed in this work, the total strain at time t_i is given by,

$$\boldsymbol{\varepsilon}(t_i) = \boldsymbol{\varepsilon}_{\mathrm{e}}(t_i) + \boldsymbol{\varepsilon}_{\mathrm{ve}}(t_i) + \boldsymbol{\varepsilon}_{\mathrm{cr}}(t_i) + \boldsymbol{\varepsilon}_{\mathrm{vp}}(t_i). \tag{A.1}$$

All the individual contributions to the total strain are subjected to the same stress tensor $\boldsymbol{\sigma}$. The expressions for these individual contributions are the same as employed in [50] and repeated here for completeness. Through the material point method, the total strains resulting from the constitutive model represented in Fig. 2 can be calculated as

$$\boldsymbol{\varepsilon}(t_i) = \underbrace{\mathbb{C}_1^{-1} : \boldsymbol{\sigma}(t_i)}_{\boldsymbol{\varepsilon}_{\mathrm{e}}(t_i)} + \underbrace{\mathbb{C}_2^{-1}(t_i) : \boldsymbol{\sigma}_0 + \sum_{j=0}^{i-1} \mathbb{C}_2^{-1}(t_i - t_j) : \Delta\boldsymbol{\sigma}_{j+1}}_{\boldsymbol{\varepsilon}_{\mathrm{ve}}(t_i)} + \underbrace{\sum_{k\in[\mathrm{cr,vp}]} \boldsymbol{\varepsilon}_k(t_{i-1}) + \Delta t\dot{\boldsymbol{\varepsilon}}_k(t_i)}_{\boldsymbol{\varepsilon}_{\mathrm{cr}}(t_i) \text{ and } \boldsymbol{\varepsilon}_{\mathrm{vp}}(t_i)} \tag{A.2}$$

where $\Delta\boldsymbol{\sigma}_{j+1} = \boldsymbol{\sigma}_{j+1} - \boldsymbol{\sigma}_j$,

$$\mathbb{C}_{ijkl}(\nu) = \frac{\nu}{(1+\nu)(1-2\nu)}\delta_{ij}\delta_{kl} + \frac{1}{2(1+\nu)}(\delta_{ik}\delta_{jl} + \delta_{il}\delta_{jk}), \tag{A.3}$$

$$\mathbb{C}_1 = E_1\mathbb{C}(\nu_1), \tag{A.4}$$

$$\mathbb{C}_2^{-1}(t) = \frac{1}{E_2}\left(1 - e^{-\frac{E_2}{\eta_2}t}\right)\mathbb{C}^{-1}(\nu_2). \tag{A.5}$$

In addition to the stress, the viscoplastic strain rate $\dot{\boldsymbol{\varepsilon}}_{\mathrm{vp}}$ also depends on the hardening parameter α, which is unknown and has to be calculated. The hardening parameter is calculated iteratively by applying Newton’s method to the residual equation of the hardening rule (Eq. (29)). In this manner, the hardening parameter at iteration $k+1$ is calculated as,

$$r_{vp}^{k+1} = r_{vp}^{k} + \left.\frac{\mathrm{d}r_{vp}}{\mathrm{d}\alpha}\right|^{k}(\alpha^{k+1} - \alpha^{k}) = 0 \quad \therefore \quad \alpha^{k+1} = \alpha^{k} - \frac{r_{vp}^{k}}{\left.\frac{\mathrm{d}r_{vp}}{\mathrm{d}\alpha}\right|^{k}}. \tag{A.6}$$

Note that the elastic and viscoelastic strains are solved exactly in Eq. (A.2). By contrast, the creep and viscoplastic strain contributions are solved numerically due to the time discretization (fully implicit formulation, in this case). However, unlike the finite element method, there are no spatial approximations in the material point solution, hence no spatial errors. For this reason, the material point method can be used to verify the finite element implementation.

Data availability

Digital data sets of the results and input data are available upon request.

References

[1] Maia TA, Barros JE, Cardoso Filho BJ, Porto MP. Experimental performance of a low cost micro-CAES generation system. Appl Energy 2016;182:358–64. http://dx.doi.org/10.1016/j.apenergy.2016.08.120.
[2] Fan J, Jiang D, Liu W, Wu F, Chen J, Daemen J. Discontinuous fatigue of salt rock with low-stress intervals. Int J Rock Mech Min Sci 2019;115:77–86. http://dx.doi.org/10.1016/j.ijrmms.2019.01.013.
[3] Rehman S, Al-Hadhrami LM, Alam MM. Pumped hydro energy storage system: A technological review. Renew Sustain Energy Rev 2015;44:586–98. http://dx.doi.org/10.1016/j.rser.2014.12.040.
[4] Khaloie H, Vallée F. Day-ahead dispatch of liquid air energy storage coupled with LNG regasification in electricity and LNG markets. IEEE Trans Power Syst 2023. http://dx.doi.org/10.1109/TPWRS.2023.3324150.
[5] Olabi A, Wilberforce T, Ramadan M, Abdelkareem MA, Alami AH. Compressed air energy storage systems: Components and operating parameters–a review. J Energy Storage 2021;34:102000. http://dx.doi.org/10.1016/j.est.2020.102000.
[6] Kumar KR, Honório H, Chandra D, Lesueur M, Hajibeygi H. Comprehensive review of geomechanics of underground hydrogen storage in depleted reservoirs and salt caverns. J Energy Storage 2023;73:108912. http://dx.doi.org/10.1016/j.est.2023.108912.

[7] Bays CA. Use of salt solution cavities for underground storage. In: Symp. salt north. ohio geol. soc. Vol. 5, 1963, p. 564–78.
[8] Lux K-H. Design of salt caverns for the storage of natural gas, crude oil and compressed air: Geomechanical aspects of construction, operation and abandonment. Geol Soc Lond Special Publ 2009;313(1):93–128. http://dx.doi.org/10.1144/SP313.7.
[9] Koenig JJ. Preparing motor gasolines for salt cavern storage of up to 10 years. SMRI Fall Mtg 1994;425.
[10] Tarkowski R, Uliasz-Misiak B, Tarkowski P. Storage of hydrogen, natural gas, and carbon dioxide–geological and legal conditions. Int J Hydrog Energy 2021;46(38):20010–22. http://dx.doi.org/10.1016/j.ijhydene.2021.03.131.
[11] Guo C, Pan L, Zhang K, Oldenburg CM, Li C, Li Y. Comparison of compressed air energy storage process in aquifers and caverns based on the Huntorf CAES plant. Appl Energy 2016;181:342–56. http://dx.doi.org/10.1016/j.apenergy.2016.08.105.
[12] Tarkowski R. Underground hydrogen storage: Characteristics and prospects. Renew Sustain Energy Rev 2019;105:86–94. http://dx.doi.org/10.1016/j.rser.2019.01.051.
[13] Tounsi H, Rutqvist J, Hu M, Wolters R, Blanco-Martín L. Numerical modeling of coupled thermal-hydro-mechanical processes in salt formations for geologic disposal of large nuclear waste canisters. In: ARMA US rock mechanics/geomechanics symposium, ARMA–2022. ARMA; 2022, http://dx.doi.org/10.56952/ARMA-2022-0794.
[14] Dusseault M, Bachu S, Rothenburg L. Sequestration of CO2 in salt caverns. J Can Pet Technol 2004;43(11). http://dx.doi.org/10.2118/04-11-04.
[15] Liu W, Dong Y, Zhang Z, Li L, Jiang D, Fan J, et al. Optimization of operating pressure of hydrogen storage salt cavern in bedded salt rock with multi-interlayers. Int J Hydrog Energy 2024;58:974–86. http://dx.doi.org/10.1016/j.ijhydene.2024.01.318.
[16] Hunsche U, Hampel A. Rock salt—the mechanical properties of the host rock material for a radioactive waste repository. Eng Geol 1999;52(3–4):271–91. http://dx.doi.org/10.1016/S0013-7952(99)00011-3.
[17] Schulze O, Popp T, Kern H. Development of damage and permeability in deforming rock salt. Eng Geol 2001;61(2–3):163–80. http://dx.doi.org/10.1016/S0013-7952(01)00051-5.
[18] Peach CJ. Influence of deformation on the fluid transport properties of salt rocks. 1991, URL http://pascal-francis.inist.fr/vibad/index.php?action=getRecordDetail&idt=19663257.
[19] Peach CJ, Spiers CJ. Influence of crystal plastic deformation on dilatancy and permeability development in synthetic salt rock. Tectonophysics 1996;256(1–4):101–28. http://dx.doi.org/10.1016/0040-1951(95)00170-0.
[20] Chan K, Bodner S, Munson D. Recovery and healing of damage in WIPP salt. Int J Damage Mech 1998;7(2):143–66. http://dx.doi.org/10.1177/105678959800700204.
[21] Zeng Z, Ma H, Yang C, Zhao K, Liang X, Li H, et al. Self-healing behaviors of damaged rock salt under humidity cycling. Int J Rock Mech Min Sci 2024;174:105636. http://dx.doi.org/10.1016/j.ijrmms.2024.105636.
[22] Munson DE. Preliminary deformation-mechanism map for salt (with application to WIPP). Tech. rep., Sandia National Lab.(SNL-NM), Albuquerque, NM (United States); 1979, http://dx.doi.org/10.2172/6499296.
[23] Urai J. Deformation mechanisms operating in naturally deformed halite rocks as deduced from microstructural investigation. Geol Mijnbouw 1987;66:165–76, URL http://pascal-francis.inist.fr/vibad/index.php?action=getRecordDetail&idt=8359566.
[24] Urai JL, Spiers CJ, Zwart HJ, Lister GS. Weakening of rock salt by water during long-term creep. Nature 1986;324(6097):554–7. http://dx.doi.org/10.1038/324554a0.
[25] Urai J, Spiers C. The effect of grain boundary water on deformation mechanisms and rheology of rocksalt during long-term deformation. In: The mechanical behavior of salt–understanding of THMC processes in salt. CRC Press; 2017, p. 149–58. http://dx.doi.org/10.1201/9781315106502.
[26] Cristescu N, Hunsche U. Time effects in rock mechanics. vol. 350, Wiley New York; 1998.
[27] Liang W, Zhao Y, Xu S, Dusseault M. Effect of strain rate on the mechanical properties of salt rock. Int J Rock Mech Min Sci 2011;48(1):161–7. http://dx.doi.org/10.1016/j.ijrmms.2010.06.012.
[28] Cristescu ND, Gioda G, et al. Visco-plastic behaviour of geomaterials. Springer; 1994, http://dx.doi.org/10.1007/978-3-7091-2710-0.
[29] Zhao K, Ma H, Zhou J, Yin H, Li P, Zhao A, et al. Rock salt under cyclic loading with high-stress intervals. Rock Mech Rock Eng 2022;55(7):4031–49. http://dx.doi.org/10.1007/s00603-022-02848-1.
[30] Lyu C, Liu J, Ren Y, Liang C, Liao Y. Study on very long-term creep tests and nonlinear creep-damage constitutive model of salt rock. Int J Rock Mech Min Sci 2021;146:104873. http://dx.doi.org/10.1016/j.ijrmms.2021.104873.
[31] Wang J, Zhang Q, Song Z, Zhang Y. Experimental study on creep properties of salt rock under long-period cyclic loading. Int J Fatigue 2021;143:106009. http://dx.doi.org/10.1016/j.ijfatigue.2020.106009.
[32] Spiers C, Schutjens P, Brzesowsky R, Peach C, Liezenberg J, Zwart H. Experimental determination of constitutive parameters governing creep of rocksalt by pressure solution. Geol Soc Lond Special Publ 1990;54(1):215–27. http://dx.doi.org/10.1144/GSL.SP.1990.054.01.21.
[33] Heusermann S, Rolfs O, Schmidt U. Nonlinear finite-element analysis of solution mined storage caverns in rock salt using the LUBBY2 constitutive model. Comput Struct 2003;81(8–11):629–38. http://dx.doi.org/10.1016/S0045-7949(02)00415-7.
[34] Hou Z. Mechanical and hydraulic behavior of rock salt in the excavation disturbed zone around underground facilities. Int J Rock Mech Min Sci 2003;40(5):725–38. http://dx.doi.org/10.1016/S1365-1609(03)00064-9.
[35] Reedlunn B. Reinvestigation into closure predictions of Room D at the Waste Isolation Pilot Plant. Tech. rep., Sandia National Lab.(SNL-NM), Albuquerque, NM (United States); 2016, http://dx.doi.org/10.2172/1333709.
[36] Munson DE, DeVries KL, Fossum AF, Callahan GD. Extension of the MD model for treating stress drops in salt. Tech. rep., Sandia National Labs.; 1993, URL https://inis.iaea.org/search/search.aspx?orig_q=RN:25002400.
[37] Reedlunn B. Enhancements to the Munson-Dawson model for rock salt. Tech. rep., Sandia National Lab.(SNL-NM), Albuquerque, NM (United States); 2018, http://dx.doi.org/10.2172/1481508.
[38] Chan KS, Bodner SR, Munson DE. Permeability of WIPP salt during damage evolution and healing. Int J Damage Mech 2001;10(4):347–75. http://dx.doi.org/10.1106/H3UV-1URA-AFUY-FX49.
[39] Maia CA, Poiate JE, Falcão JL, Coelho L. Triaxial creep tests in salt applied in drilling through thick salt layers in Campos Basin-Brazil. In: SPE/IADC drilling conference and exhibition. SPE; 2005, p. SPE–92629. http://dx.doi.org/10.2118/92629-MS.
[40] Firme PA, Brandao NB, Roehl D, Romanel C. Enhanced double-mechanism creep laws for salt rocks. Acta Geotech 2018;13:1329–40. http://dx.doi.org/10.1007/s11440-018-0689-7.
[41] Hampel A. The CDM constitutive model for the mechanical behavior of rock salt: Recent developments and extensions. In: Proceedings of the 7th conference on mechanical behaviour of salt, Paris. 2012, p. 16–9. http://dx.doi.org/10.1201/b12041.
[42] Khaledi K, Mahmoudi E, Datcheva M, Schanz T. Stability and serviceability of underground energy storage caverns in rock salt subjected to mechanical cyclic loading. Int J Rock Mech Min Sci 2016;86:115–31. http://dx.doi.org/10.1016/j.ijrmms.2016.04.010.
[43] Desai C, Varadarajan A. A constitutive model for quasi-static behavior of rock salt. J Geophys Res: Solid Earth 1987;92(B11):11445–56. http://dx.doi.org/10.1029/JB092iB11p11445.
[44] Aubertin M, Julien MR, Servant S, Gill DE. A rate-dependent model for the ductile behavior of salt rocks. Can Geotech J 1999;36(4):660–74. http://dx.doi.org/10.1139/t99-033.
[45] Cristescu N. A general constitutive equation for transient and stationary creep of rock salt. Int J Rock Mech Min Sci Geomech Abstracts 1993;30(2):125–40. http://dx.doi.org/10.1016/0148-9062(93)90705-I.
[46] Hunsche U, Schulze O. Das kriechverhalten von steinsalz. Kali und Steinsalz 1994;11(8/9):238–55.
[47] Deng J, Liu Y, Yang Q, Cui W, Zhu Y, Liu Y, et al. A viscoelastic, viscoplastic, and viscodamage constitutive model of salt rock for underground energy storage cavern. Comput Geotech 2020;119:103288. http://dx.doi.org/10.1016/j.compgeo.2019.103288.
[48] Ma L-j, Liu X-y, Fang Q, Xu H-f, Xia H-m, Li E-b, et al. A new elasto-viscoplastic damage model combined with the generalized Hoek–Brown failure criterion for bedded rock salt and its application. Rock Mech Rock Eng 2013;46:53–66. http://dx.doi.org/10.1007/s00603-012-0256-8.
[49] Zhao K, Yang C, Ma H, Daemen J. A creep-fatigue model of rock salt and its application to the deformation analysis of CAES salt caverns. Comput Geotech 2023;156:105311. http://dx.doi.org/10.1016/j.compgeo.2023.105311.
[50] Honório HT, Houben M, Bisdom K, van der Linden A, de Borst K, Sluys LJ, et al. A multi-step calibration strategy for reliable parameter determination of salt rock mechanics constitutive models. Int J Rock Mech Min Sci 2024;183:105922. http://dx.doi.org/10.1016/j.ijrmms.2024.105922.
[51] Sobolik SR, Ross TSA. Effect of the addition of a low equivalent stress mechanism to the analysis of geomechanical behavior of oil storage caverns in salt. In: ARMA US rock mechanics/geomechanics symposium. ARMA; 2021, p. ARMA–2021. http://dx.doi.org/10.2172/1870570.
[52] Buzogany R, Zander-Schiebenhöfer D, Wijermars E, den Hartogh M. Development of surface deformations above salt caverns depending on the abandonment scenario. In: The mechanical behavior of salt x. CRC Press; 2022, p. 553–66. http://dx.doi.org/10.1201/9781003295808.
[53] Firme PA, Roehl D, Romanel C. An assessment of the creep behaviour of Brazilian salt rocks using the multi-mechanism deformation model. Acta Geotech 2016;11:1445–63. http://dx.doi.org/10.1007/s11440-016-0451-y.
[54] Orlic B, Van Thienen-Visser K, Schreppers G-J. Numerical estimation of structural integrity of salt cavern wells. In: ARMA US rock mechanics/geomechanics symposium. ARMA; 2016, p. ARMA–2016, URL https://onepetro.org/ARMAUSRMS/proceedings-abstract/ARMA16/All-ARMA16/126259.
[55] Wang T, Yang C, Yan X, Daemen J. Allowable pillar width for bedded rock salt caverns gas storage. J Pet Sci Eng 2015;127:433–44. http://dx.doi.org/10.1016/j.petrol.2015.01.040.

[56] Maia da Costa A, da Costa PVM, Udebhulu OD, Cabral Azevedo R, Ebecken NF, Miranda AC, et al. Potential of storing gas with high CO2 content in salt caverns built in ultra-deep water in Brazil. Greenh Gases: Sci Technol 2019;9(1):79–94. http://dx.doi.org/10.1002/ghg.1834.

[57] Peng J, Zhou J, Liang G, Peng C, Fang S. A comprehensive stability evaluation method of multiple salt caverns underground gas storage with interlayers. Petrol Sci Technol 2022;40(13):1600–21. http://dx.doi.org/10.1080/10916466.2022.2026383.

[58] Xing W, Zhao J, Hou Z, Were P, Li M, Wang G. Horizontal natural gas caverns in thin-bedded rock salt formations. Environ Earth Sci 2015;73:6973–85. http://dx.doi.org/10.1007/s12665-015-4410-y.

[59] Coarita-Tintaya E-D, Golfier F, Grgic D, Souley M, Cheng L. Hydromechanical modelling of salt caverns subjected to cyclic hydrogen injection and withdrawal. Comput Geotech 2023;162:105690. http://dx.doi.org/10.1016/j.compgeo.2023.105690.

[60] Wang X, Wang J, Zhang Q, Song Z, Liu X, Feng S. Long-term stability analysis and evaluation of salt cavern compressed air energy storage power plant under creep-fatigue interaction. J Energy Storage 2022;55:105843. http://dx.doi.org/10.1016/j.est.2022.105843.

[61] Khaledi K, Mahmoudi E, Datcheva M, Schanz T. Analysis of compressed air storage caverns in rock salt considering thermo-mechanical cyclic loading. Environ Earth Sci 2016;75:1–17. http://dx.doi.org/10.1007/s12665-016-5970-1.

[62] Kumar KR, Hajibeygi H. Influence of pressure solution and evaporate heterogeneity on the geo-mechanical behavior of salt caverns. In: The mechanical behavior of salt x. CRC Press; 2022, p. 407–20. http://dx.doi.org/10.1201/9781003295808.

[63] Ramesh Kumar K, Makhmutov A, Spiers CJ, Hajibeygi H. Geomechanical simulation of energy storage in salt formations. Sci Rep 2021;11(1):19640. http://dx.doi.org/10.1038/s41598-021-99161-8.

[64] Pérez-Foguet A, Rodríguez-Ferran A, Huerta A. Consistent tangent matrices for substepping schemes. Comput Methods Appl Mech Engrg 2001;190(35–36):4627–47. http://dx.doi.org/10.1016/S0045-7825(00)00336-4.

[65] Wang W, Sluys L, De Borst R. Viscoplasticity for instabilities due to strain softening and strain-rate softening. Internat J Numer Methods Engrg 1997;40(20):3839–64. http://dx.doi.org/10.1002/(SICI)1097-0207(19971030)40:20<3839::AID-NME245>3.0.CO;2-6.

[66] Hangx SJ, Spiers CJ, Peach CJ. Mechanical behavior of anhydrite caprock and implications for CO2 sealing capacity. J Geophys Res: Solid Earth 2010;115(B7). http://dx.doi.org/10.1029/2009JB006954.

[67] Logg A, Mardal K-A, Wells G. Automated solution of differential equations by the finite element method: The FEniCS book. vol. 84, Springer Science & Business Media; 2012, http://dx.doi.org/10.1007/978-3-642-23099-8.

[68] Alnæs M, Blechta J, Hake J, Johansson A, Kehlet B, Logg A, et al. The FEniCS project version 1.5. Arch Numer Softw 2015;3(100). http://dx.doi.org/10.11588/ans.2015.100.20553.

[69] Geuzaine C, Remacle J-F. Gmsh: A 3-D finite element mesh generator with built-in pre-and post-processing facilities. Int J Numer Methods Eng 2009;79(11):1309–31. http://dx.doi.org/10.1002/nme.2579.

[70] Dalcin LD, Paz RR, Kler PA, Cosimo A. Parallel distributed computing using python. Adv Water Resour 2011;34(9):1124–39. http://dx.doi.org/10.1016/j.advwatres.2011.04.013.

[71] Yin H, Yang C, Ma H, Shi X, Zhang N, Ge X, et al. Stability evaluation of underground gas storage salt caverns with micro-leakage interlayer in bedded rock salt of Jintan, China. Acta Geotech 2020;15:549–63. http://dx.doi.org/10.1007/s11440-019-00901-y.

[72] Cofrade G, Závada P, Krÿza O, Cantarero I, Gratacós Ò, Ferrer O, et al. The kinematics of a salt sheet recorded in an array of distorted intrasalt stringers (Les Avellanes Diapir–South-Central Pyrenees). J Struct Geol 2023;176:104963. http://dx.doi.org/10.1016/j.jsg.2023.104963.